J. Plasma Phys. (2019), *vol.* 85, 795850501 © Cambridge University Press 2019
doi:10.1017/S0022377819000527

An adjoint method for neoclassical stellarator optimization

Elizabeth J. Paul[1,†], **Ian G. Abel**[1,2], **Matt Landreman**[1] and **William Dorland**[1]

[1]Institute for Research in Electronics and Applied Physics, University of Maryland, College Park, MD 20742, USA

[2]Department of Physics, Chalmers University of Technology, Göteborg, SE-41296, Sweden

(Received 12 April 2019; revised 6 July 2019; accepted 8 July 2019)

Stellarators are a promising route to steady-state fusion power. However, to achieve the required confinement, the magnetic geometry must be highly optimized. This optimization requires navigating high-dimensional spaces, often necessitating the use of gradient-based methods. The gradient of the neoclassical fluxes is expensive to compute with classical methods, requiring $O(N)$ flux computations, where N is the number of parameters. To reduce the cost of the gradient computation, we present an adjoint method for computing the derivatives of moments of the neoclassical distribution function for stellarator optimization. The linear adjoint method allows derivatives of quantities which depend on solutions of a linear system, such as moments of the distribution function, to be computed with respect to many parameters from the solution of only two linear systems. This reduces the cost of computing the gradient to the point that the finite-collisionality neoclassical fluxes can be used within an optimization loop. With the neoclassical adjoint method, we compute solutions of the drift kinetic equation and an adjoint drift kinetic equation to obtain derivatives of neoclassical quantities with respect to geometric parameters. When the number of parameters in the derivative is large ($O(10^2)$), this adjoint method provides up to a factor of 200 reduction in cost. We demonstrate adjoint-based optimization of the field strength to obtain minimal bootstrap current on a surface. With adjoint-based derivatives, we also compute the local sensitivity to magnetic perturbations on a flux surface and identify regions where tight tolerances on error fields are required for control of the bootstrap current or radial transport. Furthermore, the solve for the ambipolar electric field is accelerated using a Newton method with derivatives obtained from the adjoint method.

Key words: fusion plasma, plasma confinement, plasma simulation

1. Introduction

The stellarator is a promising approach to magnetic confinement, as it does not require plasma current to produce rotational transform and thus is inherently steady state and stable to current-driven modes. However, collisionless trajectories are not

† Email address for correspondence: ejpaul@umd.edu

https://doi.org/10.1017/S0022377819000527 Published online by Cambridge University Press

guaranteed to be confined in three-dimensional geometry as they are in axisymmetric systems (Gibson & Taylor 1967; Helander 2014). This can lead to poor confinement of energetic particles and increased neoclassical transport. A possible solution is the application of numerical optimization techniques to carefully tailor the magnetic geometry for improved confinement properties. One of the first demonstrations of this technique was in the design of the Wendelstein 7-X (W7-X) stellarator (Grieger *et al.* 1992; Lotz, Nührenberg & Schwab 1990), which was optimized for small neoclassical transport in the $1/\nu$ regime and for small bootstrap current, in addition to several other physics criteria.

Another approach to improve confinement in stellarators is to obtain a configuration whose magnetic field strength exhibits a symmetry direction when expressed in Boozer coordinates, known as quasi-symmetry (Nührenberg & Zille 1988). This leads to a conserved canonical momentum of the guiding centre motion such that neoclassical properties are similar to those in a tokamak. However, perfect quasi-symmetry can never be achieved globally in practice (Garren & Boozer 1991; Landreman & Sengupta 2018), and it is often desirable to include symmetry-breaking components of the magnetic field strength in consideration of other design parameters, such as magneto-hydrodynamic (MHD) stability and energetic particle confinement (Nelson *et al.* 2003; Henneberg *et al.* 2019). As one must allow for breaking of quasi-symmetry, it remains essential to include a measure of neoclassical transport such that the symmetry-breaking harmonics of the field strength do not significantly degrade the confinement.

Neoclassical transport is governed by solutions of the drift kinetic equation, (DKE) (2.1), from which moments (e.g. radial fluxes and bootstrap current) are computed. The DKE local to a flux surface can be solved numerically (Landreman *et al.* 2014; Belli & Candy 2015). However, this four-dimensional problem is expensive to solve within an optimization loop, especially in low-collisionality regimes for which increased pitch-angle resolution is required in the collisional boundary layer.

Therefore, it may be desirable to consider an analytic reduction of the DKE. Under the assumption of low collisionality, a bounce-averaged DKE can be considered (Beidler & D'haeseleer 1995; Calvo *et al.* 2018). While bounce averaging can significantly reduce the computational cost by decreasing the spatial dimensionality, this approach typically requires restrictions on the geometry, such as closeness to omnigeneity or a model magnetic field. Additional reduction of the DKE can be made in low-collisionality regimes, resulting in semi-analytic expressions. For example the effective ripple, ϵ_{eff} (Nemov *et al.* 1999), quantifies the geometric dependence of the $1/\nu$ radial transport, where ν is the collision frequency, and has been widely used during optimization studies (Zarnstorff *et al.* 2001; Ku *et al.* 2008; Henneberg *et al.* 2019). This model, though, assumes very small values of the radial electric field, E_r, which is not always an experimentally relevant regime. A low-collisionality semi-analytic bootstrap current model (Shaing *et al.* 1989) is also commonly adopted for stellarator design (Beidler *et al.* 1990; Hirshman *et al.* 1999). However, this analytic expression is known to be ill-behaved near rational surfaces. Furthermore, benchmarks with numerical solutions of the DKE in the low-collisionality limit have been shown to differ significantly from the semi-analytic model (Beidler *et al.* 2011; Kernbichler *et al.* 2016). Any analytic reduction of the DKE implies additional assumptions, such as on the collisionality, size of E_r, or on the magnetic geometry.

Due to the limitations of bounce-averaged and semi-analytic models, there are benefits to computing neoclassical quantities using numerical solutions to the DKE without approximation. With the numerical methods currently used for

https://doi.org/10.1017/S0022377819000527 Published online by Cambridge University Press

stellarator optimization, this approach becomes computationally challenging within an optimization loop. Due to their fully three-dimensional nature, optimization of stellarator geometry requires navigation through high-dimensional spaces, such as the space of the shape of the outer boundary of the plasma or the shapes of electromagnetic coils. The number of parameters required to describe these spaces, N, is often quite large ($O(10^2)$). Knowledge of the gradient of the objective function with respect to these parameters can greatly improve the convergence to a local minimum. Once a descent direction is identified, each iteration reduces to a one-dimensional line search. Gradient-based optimization with the Levenberg–Marquardt algorithm in the STELLOPT code (Strickler *et al.* 2004) has been widely used in the stellarator community and led to the design of the National Compact Stellarator Experiment, NCSX (Reiman *et al.* 1999).

Although derivative information is valuable, numerically computing the derivative of a figure of merit f (for example, with finite difference derivatives) can be prohibitively expensive, as f must be evaluated $O(N)$ times. For neoclassical optimization, this implies solving the DKE $O(N)$ times; thus including finite-collisionality neoclassical quantities in the objective function is often impractical. In this work we describe an adjoint method for neoclassical optimization. With this method, the computation of the derivatives of f with respect to N parameters has cost comparable to solving the DKE twice, thus making the inclusion of these quantities possible within an optimization loop. In this work we obtain derivatives of neoclassical figures of merit with respect to local geometric parameters on a surface rather than the outer boundary or coil shapes. However, the geometric derivatives we compute provide an important step toward adjoint-based optimization of MHD equilibria, as discussed in § 5.2.2.

Adjoint methods have been applied in many fields including aerodynamic engineering and computational fluid dynamics (Pironneau 1974; Glowinski & Pironneau 1975), geophysics (Fichtner, Bunge & Igel 2006; Plessix 2006), structural engineering (Allaire *et al.* 2005) and tokamak divertor design (Dekeyser, Reiter & Baelmans 2014*a*,*b*,*c*). They have only recently been implemented for stellarator design, namely for the design of coil shapes (Paul *et al.* 2018) and efficiently computing shape gradients for MHD equilibria (Antonsen, Paul & Landreman 2019). The numerical method is quite general and has the potential to greatly impact many inverse design problems in magnetic confinement fusion.

In § 2 we provide an overview of the numerical solution of the DKE local to a flux surface. In § 3 the adjoint neoclassical method is described. Two approaches to the adjoint method, termed continuous and discrete, are presented, and their implementation and benchmarks are discussed in § 4. The adjoint method is used to compute derivatives of moments of the neoclassical distribution function with respect to local geometric quantities. The derivative information can be used to identify regions of increased sensitivity to magnetic perturbations, as discussed in § 5.1. We demonstrate adjoint-based optimization in § 5.2.1 by locally modifying the field strength on a flux surface. A discussion of the application of this method for optimization of MHD equilibria is presented in 5.2.2. Finally, the adjoint method is applied to accelerate the calculation of the ambipolar electric field in § 5.3.

2. Drift kinetic equation

The stellarator Fokker–Planck iterative neoclassical solver (SFINCS) code (Landreman *et al.* 2014) solves the drift kinetic equation,

$$(v_\parallel \boldsymbol{b} + \boldsymbol{v}_E) \cdot \nabla f_{1s} - C_s(f_{1s}) = -\boldsymbol{v}_{\mathrm{ms}} \cdot \nabla \psi \frac{\partial f_{Ms}}{\partial \psi}, \tag{2.1}$$

https://doi.org/10.1017/S0022377819000527 Published online by Cambridge University Press

for general stellarator geometry. Here $\boldsymbol{b} = \boldsymbol{B}/B$ is a unit vector in the direction of the magnetic field, $v_\parallel = \boldsymbol{v} \cdot \boldsymbol{b}$ is the parallel component of the velocity and $2\pi\psi$ is the toroidal flux. The Fokker–Planck collision operator is $C_s(f_{1s})$, linearized about a Maxwellian $f_{Ms} = n_s v_{ts}^{-3} \pi^{-3/2} \mathrm{e}^{-v^2/v_{ts}^2}$ where $v_{ts} = \sqrt{2T_s/m_s}$ is the thermal speed, n_s is the density, T_s is the temperature, m_s is the mass and the subscript indicates species. In (2.1), derivatives are performed holding $W_s = m_s v^2/2 + q_s \Phi$ and $\mu = v_\perp^2/2B$ fixed, where $v = \sqrt{\boldsymbol{v} \cdot \boldsymbol{v}}$ is the magnitude of velocity, Φ is the electrostatic potential, $v_\perp = \sqrt{v^2 - v_\parallel^2}$ is the perpendicular velocity and q_s is the charge. The radial magnetic drift is

$$\boldsymbol{v}_{\mathrm{m}s} \cdot \nabla\psi = \frac{m_s}{q_s B^2} \left(v_\parallel^2 + \frac{v_\perp^2}{2} \right) \boldsymbol{b} \times \nabla B \cdot \nabla\psi, \tag{2.2}$$

assuming a magnetic field in MHD force balance, and $\boldsymbol{v}_E$ is the $\boldsymbol{E} \times \boldsymbol{B}$ velocity

$$\boldsymbol{v}_E = \frac{\boldsymbol{B} \times \nabla\Phi}{B^2}. \tag{2.3}$$

Throughout we assume $\Phi = \Phi(\psi)$ such that (2.1) is linear. In (2.1) we will not consider the effect of inductive electric fields, as this can be assumed to be small for stellarators without inductive current drive. We also do not consider the effects of magnetic drifts tangential to the flux surface in (2.1), as these only become important when E_r is small (Paul *et al.* 2017).

SFINCS solves (2.1) locally on a flux surface ψ, thus it is four-dimensional. The SFINCS coordinates include two angles (poloidal angle θ and toroidal angle ζ), speed $x_s = v/v_{ts}$ and pitch angle $\xi_s = v_\parallel/v$. Specifics about the implementation of (2.1) in the SFINCS code are described in appendix A. We will refer to two choices of implementation, the full trajectory model and the DKES trajectory model. The DKES model is employed in the drift kinetic equation solver (DKES) (van Rij & Hirshman 1989). The full trajectory model maintains μ conservation as radial coupling (terms involving $\partial f_{1s}/\partial\psi$) is dropped. While the DKES model does not conserve μ when the radial electric field $E_r \neq 0$, the adjoint operator under the DKES model takes a particularly simple form as discussed in § 3.1. This model also does not introduce any unphysical constraints on the distribution function when $E_r = 0$, as occurs for the full trajectory model (Landreman *et al.* 2014). These constraints motivate the introduction of particle and heat sources, which are discussed in the following section. We will discuss some of the details of the implementation of the DKE in the SFINCS code as these need to be considered in arriving at the adjoint equation. However, the adjoint neoclassical approach is quite general and could be implemented in other drift kinetic codes with slight modification.

From solutions of (2.1), several neoclassical quantities are computed, including the flux surface-averaged parallel flow,

$$V_{\parallel,s} = \frac{\left\langle B \int \mathrm{d}^3 v \, f_{1s} v_\parallel \right\rangle_\psi}{n_s \langle B^2 \rangle_\psi^{1/2}}, \tag{2.4}$$

the radial particle flux,

$$\Gamma_s = \left\langle \int \mathrm{d}^3 v \, (\boldsymbol{v}_{\mathrm{m}s} \cdot \nabla\rho) f_{1s} \right\rangle_\psi, \tag{2.5}$$

https://doi.org/10.1017/S0022377819000527 Published online by Cambridge University Press

and the radial heat flux (sometimes referred to as an energy flux),

$$Q_s = \left\langle \int \mathrm{d}^3 v \, \frac{m_s v^2}{2} (\boldsymbol{v}_{\mathrm{ms}} \cdot \nabla \rho) f_{1s} \right\rangle_{\psi}. \tag{2.6}$$

We will also consider species-summed quantities including the bootstrap current, $J_b = \sum_s q_s n_s V_{\parallel,s}$, the radial current, $J_r = \sum_s q_s \Gamma_s$, and the total heat flux, $Q_{\mathrm{tot}} = \sum_s Q_s$. Here the effective normalized radius is $\rho = \sqrt{\psi/\psi_0}$, where $2\pi\psi_0$ is the toroidal flux at the boundary.

2.1. *Sources and constraints*

To avoid unphysical constraints on f_{1s} implied by the moment equations of (2.1) in the presence of a non-zero E_r (Landreman *et al.* 2014), particle and heat sources are added to the DKE (A 1),

$$\mathbb{L}_{0s} f_{1s} - C_s(f_{1s}) - f_{Ms}(x_s^2 - \tfrac{5}{2}) S_{1s}^f(\psi) - f_{Ms}(x_s^2 - \tfrac{3}{2}) S_{2s}^f(\psi) = \mathbb{S}_{0s}, \tag{2.7}$$

where $S_{1s}^f(\psi)$ and $S_{2s}^f(\psi)$ are unknowns such that S_{1s}^f provides a particle source and S_{2s}^f provides a heat source. The collisionless trajectory operator in SFINCS coordinates is

$$\mathbb{L}_{0s} = \dot{\boldsymbol{r}} \cdot \nabla + \dot{x}_s \frac{\partial}{\partial x_s} + \dot{\xi}_s \frac{\partial}{\partial \xi_s}, \tag{2.8}$$

and the inhomogeneous drive term is $\mathbb{S}_{0s} = -(\boldsymbol{v}_{\mathrm{ms}} \cdot \nabla \psi) \partial f_{Ms} / \partial \psi$. The source functions are determined via the requirement that $\langle \int \mathrm{d}^3 v f_{1s} \rangle_\psi = 0$ and $\langle \int \mathrm{d}^3 v \, x_s^2 f_{1s} \rangle_\psi = 0$ (i.e. f_{1s} does not provide net density or pressure). So, the following system of equations is solved,

$$\underbrace{\begin{bmatrix} \mathbb{L}_{0s} - C_s & -f_{Ms}(x_s^2 - \frac{5}{2}) & -f_{Ms}(x_s^2 - \frac{3}{2}) \\ \mathbb{L}_{1s} & 0 & 0 \\ \mathbb{L}_{2s} & 0 & 0 \end{bmatrix}}_{\mathbb{L}_s} \underbrace{\begin{bmatrix} f_{1s} \\ S_{1s}^f \\ S_{2s}^f \end{bmatrix}}_{F_s} = \underbrace{\begin{bmatrix} \mathbb{S}_{0s} \\ 0 \\ 0 \end{bmatrix}}_{\mathbb{S}_s}. \tag{2.9}$$

The velocity-space averaging operations are denoted $\mathbb{L}_{1s} f_{1s} = \langle \int \mathrm{d}^3 v f_{1s} \rangle_\psi$ and $\mathbb{L}_{2s} f_{1s} = \langle \int \mathrm{d}^3 v f_{1s} x_s^2 \rangle_\psi$. The full multi-species system can be written as,

$$\begin{bmatrix} \mathbb{L}_1 & & \\ & \ddots & \\ & & \mathbb{L}_{N_{\mathrm{species}}} \end{bmatrix} \begin{bmatrix} F_1 \\ \vdots \\ F_{N_{\mathrm{species}}} \end{bmatrix} = \begin{bmatrix} \mathbb{S}_1 \\ \vdots \\ \mathbb{S}_{N_{\mathrm{species}}} \end{bmatrix}. \tag{2.10}$$

Here the linear systems corresponding to each species as in (2.9) are coupled through the collision operator. We use the following notation to refer to the above system,

$$\mathbb{L} F = \mathbb{S}. \tag{2.11}$$

https://doi.org/10.1017/S0022377819000527 Published online by Cambridge University Press

3. Adjoint approach

The goal of the adjoint neoclassical approach is to efficiently compute derivatives of a moment of the distribution function, $\mathcal{R}$ (e.g. $V_{\parallel,s}$, Γ_s, Q_s, J_b, J_r, Q_{tot}), with respect to many parameters. Consider a set of parameters, $\Omega = \{\Omega_i\}_{i=1}^{N_\Omega}$, on which $\mathcal{R}$ depends. Computing a forward difference derivative with respect to Ω requires $N_\Omega + 1$ solutions of (2.11). With the adjoint approach, $\partial\mathcal{R}/\partial\Omega$ can be computed with one solution of (2.11) and one solution of a linear adjoint equation of the same size as (2.11). Thus if N_Ω is very large and the solution to (2.11) is computationally expensive to obtain, the adjoint approach can reduce the cost by a factor of N_Ω. For stellarator optimization, it is desirable to compute derivatives with respect to parameters which describe the magnetic geometry. In fully three-dimensional geometry, N_Ω is $O(10^2)$ and solving (2.11) is the most expensive part of computing $\mathcal{R}$ (rather than constructing the linear system or taking a moment of the distribution function). Thus the adjoint approach can provide a computational savings of a factor of $O(10^2)$. The adjoint method is also advantageous over numerical derivatives, as it avoids additional noise from discretization error. In what follows we consider Ω to be a set of parameters describing the magnetic geometry, which will be specified in § 4.

We compute the derivatives of $\mathcal{R}$ using two approaches. In the first approach, we define an inner product which involves integrals over the distribution function, and an adjoint operator is obtained with respect to this inner product. This we refer to as the continuous approach. In the second approach, we consider the DKE after discretization, defining an adjoint operator with respect to the Euclidean dot product. This we refer to as the discrete approach. While these approaches should provide identical results within discretization error, the advantages and drawbacks of each approach will be discussed at the end of § 3.2.

3.1. *Continuous approach*

Let $F = \{F_s\}_{s=1}^{N_{\text{species}}}$ be the set of unknowns computed with SFINCS before discretization, denoted by the column vector in (2.10) with F_s given by (2.9). That is, F consists of a set of N_{species} distribution functions over $(\theta, \zeta, x_s, \xi_s)$ and their associated source functions. We define an inner product between two such quantities in the following way,

$$\langle F, G\rangle = \sum_s \left\langle \int \mathrm{d}^3 v \, \frac{f_{1s} g_{1s}}{f_{Ms}} \right\rangle_\psi + S^f_{1s} S^g_{1s} + S^f_{2s} S^g_{2s}. \tag{3.1}$$

Here the superscript on S_{1s} and S_{2s} denotes the distribution function with which the source functions are associated and the sum is over species. The space of continuous functions, F, of this form such that $\langle F, F\rangle$ is bounded will be denoted by $\mathcal{H}$. It can be seen that (3.1) is indeed an inner product, as it satisfies conjugate symmetry ($\langle G, F\rangle = \langle F, G\rangle \ \forall F, G \in \mathcal{H}$), linearity ($\langle F + G, H\rangle = \langle F, H\rangle + \langle G, H\rangle \ \forall F, G, H \in \mathcal{H}$ and $\langle F, aG\rangle = a\langle F, G\rangle \ \forall F, G \in \mathcal{H}, a \in \mathbb{R}$), and positive definiteness ($\langle F, F\rangle \geqslant 0$ and $\langle F, F\rangle = 0$ only if $F = 0 \ \forall F \in \mathcal{H}$) (Rudin 2006). This implies that if $\mathcal{H}$ is finite-dimensional, then for any linear operator L there exists a unique adjoint operator $L^\dagger$ such that $\langle LF, G\rangle = \langle F, L^\dagger G\rangle$ for all $F, G \in \mathcal{H}$. While here $\mathcal{H}$ is not finite-dimensional, we will show that such an adjoint operator exists for this inner product.

Note that the norm associated with this inner product $\|F\| = \sqrt{\langle F, F\rangle}$ is similar to the free energy norm,

$$W = \sum_s \left\langle \int \mathrm{d}^3 v \, \frac{T_s f_{1s}^2}{2 f_{Ms}} \right\rangle_\psi, \tag{3.2}$$

https://doi.org/10.1017/S0022377819000527 Published online by Cambridge University Press

which obeys a conservation equation in gyrokinetic theory (Krommes & Hu 1994; Abel *et al.* 2013; Landreman, Plunk & Dorland 2015). The choice of inner product (3.1) is advantageous, as the linearized Fokker–Planck collision operator becomes self-adjoint for species linearized about Maxwellians with the same temperature. In what follows, we assume that all included species are of the same temperature. This assumption could be lifted, with a modification to the collision operator that appears in the adjoint equation (see appendix B). This assumption is not necessary when using the discrete approach (see § 3.2).

Consider a moment of the distribution function $\mathcal{R} \in \{V_{\parallel,s}, \Gamma_s, Q_s, J_b, J_r, Q_{\text{tot}}\}$, which can be written as an inner product with a vector $\widetilde{\mathcal{R}} \in \mathcal{H}$,

$$\mathcal{R} = \langle F, \widetilde{\mathcal{R}} \rangle, \tag{3.3}$$

according to (3.1). For example,

$$\widetilde{J_r} = \begin{bmatrix} q_s \boldsymbol{v}_{\text{m}s} \cdot \boldsymbol{\nabla} \psi f_{Ms} \\ 0 \\ 0 \end{bmatrix}_{s=1}^{N_{\text{species}}}, \tag{3.4}$$

where the column structure corresponds with that in (2.9) and (2.10).

We are interested in computing the derivative of $\mathcal{R}$ with respect to a set of parameters, $\Omega = \{\Omega_i\}_{i=1}^{N_\Omega}$. This derivative can be computed with the chain rule,

$$\left(\frac{\partial \mathcal{R}}{\partial \Omega_i}\right)_{\mathbb{L}F=\mathbb{S}} = \left(\frac{\partial \mathcal{R}}{\partial \Omega_i}\right)_F + \left\langle \widetilde{\mathcal{R}}, \left(\frac{\partial F}{\partial \Omega_i}\right)_{\mathbb{L}F=\mathbb{S}} \right\rangle. \tag{3.5}$$

The subscripts in (3.5) denote the quantity that is held fixed while the derivative is computed. The first term on the right-hand side accounts for the explicit dependence on Ω_i while the second accounts for the implicit dependence on Ω_i through F. Here $(\partial F/\partial \Omega_i)_{\mathbb{L}F=\mathbb{S}}$ can be computed by considering perturbations to the linear system (2.11), noting that in general both $\mathbb{L}$ and $\mathbb{S}$ can depend on Ω,

$$\mathbb{L}\left(\frac{\partial F}{\partial \Omega_i}\right)_{\mathbb{L}F=\mathbb{S}} = \left(\frac{\partial \mathbb{S}}{\partial \Omega_i} - \frac{\partial \mathbb{L}}{\partial \Omega_i} F\right). \tag{3.6}$$

Computing $(\partial F/\partial \Omega)_{\mathbb{L}F=\mathbb{S}}$ using (3.6) requires solving N_Ω linear systems of the same dimension as the DKE (2.11). To avoid this additional computational cost, we instead solve an adjoint equation,

$$\mathbb{L}^\dagger q^{\mathcal{R}} = \widetilde{\mathcal{R}}. \tag{3.7}$$

In what follows, we show that the adjoint variable, $q^{\mathcal{R}}$, can be used to compute $(\partial \mathcal{R}/\partial \Omega)_{\mathbb{L}F=\mathbb{S}}$ without solving (3.6) for each Ω_i. Using (3.7) with (3.5),

$$\left(\frac{\partial \mathcal{R}}{\partial \Omega_i}\right)_{\mathbb{L}F=\mathbb{S}} = \left(\frac{\partial \mathcal{R}}{\partial \Omega_i}\right)_F + \left\langle \mathbb{L}^\dagger q^{\mathcal{R}}, \left(\frac{\partial F}{\partial \Omega_i}\right)_{\mathbb{L}F=\mathbb{S}} \right\rangle, \tag{3.8}$$

and applying the adjoint property, we obtain

$$\left(\frac{\partial \mathcal{R}}{\partial \Omega_i}\right)_{\mathbb{L}F=\mathbb{S}} = \left(\frac{\partial \mathcal{R}}{\partial \Omega_i}\right)_F + \left\langle q^{\mathcal{R}}, \mathbb{L}\left(\frac{\partial F}{\partial \Omega_i}\right)_{\mathbb{L}F=\mathbb{S}} \right\rangle. \tag{3.9}$$

https://doi.org/10.1017/S0022377819000527 Published online by Cambridge University Press

Using (3.6),

$$\left(\frac{\partial \mathcal{R}}{\partial \Omega_i}\right)_{\mathbb{L}F=\mathbb{S}} = \left(\frac{\partial \mathcal{R}}{\partial \Omega_i}\right)_F + \left\langle q^{\mathcal{R}}, \left(\frac{\partial \mathbb{S}}{\partial \Omega_i} - \frac{\partial \mathbb{L}}{\partial \Omega_i} F\right)\right\rangle. \tag{3.10}$$

So, (3.10) provides the same derivative information as (3.5). Thus, using (3.10), the derivative with respect to Ω can be computed with the solution to two linear systems, (2.11) and (3.7). The partial derivatives on the right-hand side of (3.10) can be computed analytically by considering the explicit geometric dependence of $\mathcal{R}$, $\mathbb{L}$ and $\mathbb{S}$.

When N_Ω is large, the cost of computing $\partial\mathcal{R}/\partial\Omega$ using (3.10) is dominated not by the linear solve but by constructing $\partial\mathbb{S}/\partial\Omega$ and $\partial\mathbb{L}/\partial\Omega$ and computing the inner product. Thus the cost still scales with N_Ω. However, we obtain a significant savings in comparison with forward difference derivatives, as shown in § 4.

The adjoint operator for each species takes the following form,

$$\mathbb{L}_s^\dagger = \begin{bmatrix} \mathbb{L}_{0s}^\dagger - C_s & f_{Ms} & f_{Ms}x^2 \\ \mathbb{L}_{1s}^\dagger & 0 & 0 \\ \mathbb{L}_{2s}^\dagger & 0 & 0 \end{bmatrix}, \tag{3.11}$$

where $\mathbb{L}_{1s}^\dagger = 5/2\mathbb{L}_{1s} - \mathbb{L}_{2s}$ and $\mathbb{L}_{2s}^\dagger = 3/2\mathbb{L}_{1s} - \mathbb{L}_{2s}$. The same column structure is used as for the forward operator (2.10), $\mathbb{L}^\dagger = \{\mathbb{L}_s^\dagger\}_{i=1}^{N_{\text{species}}}$. The quantity $\mathbb{L}_{0s}^\dagger$ satisfies $\langle \int \mathrm{d}^3v\, g_{1s}\mathbb{L}_{0s}f_{1s}/f_{Ms}\rangle_\psi = \langle \int \mathrm{d}^3v f_{1s}\mathbb{L}_{0s}^\dagger g_{1s}/f_{Ms}\rangle_\psi$ and depends on which trajectory model is applied. The expression (3.11) can be verified by noting that

$$\begin{aligned}\langle \mathbb{L}F, G\rangle &= \sum_s \left\langle \frac{f_{1s}((\mathbb{L}_{0s}^\dagger - C_s)g_{1s} + f_{Ms}(S_{1s}^g + S_{2s}^g x_s^2))}{f_{Ms}} \right\rangle_\psi + S_{1s}^f \mathbb{L}_{1s}^\dagger g_{1s} + S_{2s}^f \mathbb{L}_{2s}^\dagger g_{1s} \\ &= \langle F, \mathbb{L}^\dagger G\rangle. \end{aligned} \tag{3.12}$$

For the DKES trajectories the adjoint operator is,

$$\mathbb{L}_{0s}^\dagger = -\mathbb{L}_{0s}. \tag{3.13}$$

This anti-self-adjoint property is used in obtaining the variational principle which provides bounds on neoclassical transport coefficients in the DKES code (van Rij & Hirshman 1989). For full trajectories it is,

$$\mathbb{L}_{0s}^\dagger = -\mathbb{L}_{0s} + \frac{q_s}{T_s}\frac{\mathrm{d}\Phi}{\mathrm{d}\psi}\boldsymbol{v}_{\mathrm{ms}} \cdot \nabla\psi. \tag{3.14}$$

The anti-self-adjoint property does not hold for this trajectory model as the $\boldsymbol{E}\times\boldsymbol{B}$ drift (C 9) is no longer divergenceless. See appendix C for details on obtaining these adjoint operators.

3.2. *Discrete approach*

Next we consider the discrete adjoint approach. Let $\vec{F}$ be the set of unknowns computed with SFINCS after discretization of F. The linear DKE (2.11) upon discretization can then be written schematically as

$$\overleftrightarrow{L}\,\vec{F} = \vec{S}. \tag{3.15}$$

https://doi.org/10.1017/S0022377819000527 Published online by Cambridge University Press

In this case, we can define an inner product as the vector dot product,

$$\langle \vec{F}, \vec{G} \rangle = \vec{F} \cdot \vec{G}. \tag{3.16}$$

In real Euclidean space, the adjoint operator, $(\overleftrightarrow{L})^\dagger$, which satisfies

$$\langle \overleftrightarrow{L}\,\vec{F}, \vec{G} \rangle = \langle \vec{F}, (\overleftrightarrow{L})^\dagger \vec{G} \rangle \tag{3.17}$$

is simply the transpose of the matrix, $(\overleftrightarrow{L})^{\mathrm{T}}$. Again, the moments of the distribution function, $\mathcal{R}$ can be expressed as an inner product with a vector $\vec{R}$,

$$\mathcal{R} = \langle \vec{F}, \vec{R} \rangle. \tag{3.18}$$

Using the discrete approach, the following adjoint equation must be solved

$$(\overleftrightarrow{L})^{\mathrm{T}} \vec{q}^{\,\mathcal{R}} = \vec{R}. \tag{3.19}$$

The adjoint variable, $\vec{q}^{\,\mathcal{R}}$, can again be used to compute $(\partial \mathcal{R}/\partial \Omega_i)_{\overleftrightarrow{L}\vec{F}=\vec{S}}$,

$$\left(\frac{\partial \mathcal{R}}{\partial \Omega_i}\right)_{\overleftrightarrow{L}\vec{F}=\vec{S}} = \left(\frac{\partial \mathcal{R}}{\partial \Omega_i}\right)_{\vec{F}} + \left\langle \vec{q}^{\,\mathcal{R}}, \left(\frac{\partial \vec{S}}{\partial \Omega_i} - \frac{\partial \overleftrightarrow{L}}{\partial \Omega_i}\vec{F}\right) \right\rangle. \tag{3.20}$$

As with the continuous approach, the partial derivatives on the right-hand side can be computed analytically. In this way, the derivative of $\mathcal{R}$ with respect to Ω can be computed with only two linear solves, (3.15) and (3.19).

In the SFINCS implementation, the DKE is typically solved with the preconditioned GMRES algorithm. In the continuous approach, a preconditioner matrix for both the forward and adjoint operator must be lower–upper (LU)-factorized. Here the preconditioner matrix is the same as the full matrix but without cross-species or speed coupling. As the adjoint matrix is sufficiently different from the forward matrix, we do not obtain convergence when the same preconditioner is used for both problems. However, in the discrete approach, the LU-factorization for the preconditioner of the forward matrix can be reused for the preconditioner of the adjoint matrix (If a matrix $\boldsymbol{A}$ has been factorized as $\boldsymbol{A} = LU$ then $\boldsymbol{A}^{\mathrm{T}} = U^{\mathrm{T}}L^{\mathrm{T}}$ where U^{T} is lower triangular and L^{T} is upper triangular). This provides a significant reduction in memory and computational cost for the discrete approach.

Furthermore, the discrete adjoint approach provides the exact derivatives for the discretized problem. With this method the adjoint equation is obtained using the vector dot product and matrix transpose which can be computed without any numerical approximation. The error in the derivatives obtained by the adjoint method are therefore only limited by the tolerance to which the linear solve is performed with GMRES. On the other hand, the continuous adjoint approach relies on a continuous inner product which must ultimately be approximated numerically. Thus the continuous approach provides the exact derivatives only in the limit that the discrete approximation of the inner product exactly reproduces the continuous inner product. Therefore we expect the results of the discrete and adjoint approaches to agree within discretization error, as will be demonstrated in § 4.

The continuous approach can be advantageous in that an adjoint equation may be prescribed independently of the discretization scheme. Note that in the discrete approach, the adjoint operator is obtained from the matrix transpose of the discretized forward operator, which implies that the same spatial and velocity resolution parameters must be used for both the forward and adjoint solutions. In this work we will employ the same discretization parameters for both the adjoint and forward problems, but this restriction is not required for the continuous approach.

https://doi.org/10.1017/S0022377819000527 Published online by Cambridge University Press

4. Implementation and benchmarks

The adjoint method has been implemented in the SFINCS code using both the discrete and continuous approaches. The magnetic geometry is specified in Boozer coordinates (Helander 2014) such that the covariant form of the magnetic field is,

$$\boldsymbol{B} = I(\psi)\nabla\theta + G(\psi)\nabla\zeta + K(\psi, \theta, \zeta)\nabla\psi, \tag{4.1}$$

where $I(\psi) = \mu_0 I_T(\psi)/2\pi$ and $G(\psi) = \mu_0 I_P(\psi)/2\pi$, $I_T(\psi)$ is the toroidal current enclosed by ψ, and $I_P(\psi)$ is the poloidal current outside of ψ. The contravariant form is

$$\boldsymbol{B} = \nabla\psi \times \nabla\theta - \iota(\psi)\nabla\psi \times \nabla\zeta, \tag{4.2}$$

where $\iota(\psi)$ is the rotational transform. The Jacobian is obtained from dotting (4.1) with (4.2),

$$\sqrt{g} = \frac{G(\psi) + \iota(\psi)I(\psi)}{B^2}. \tag{4.3}$$

As $K(\psi, \theta, \zeta)$ does not appear in any of the trajectory coefficients ((A 2) and (A 5)), in the drive term in (A 1), or in the geometric factors used to define the moments of the distribution function ((2.4) to (2.6)), all the geometric dependence enters through $B(\psi, \theta, \zeta)$, $G(\psi)$, $I(\psi)$ and $\iota(\psi)$. We choose to use Boozer coordinates for these computations as it reduces the number of geometric parameters that must be considered, but the neoclassical adjoint method is not limited to this choice of coordinate system.

We approximate B by a truncated Fourier series,

$$B = \sum_j B^c_{m_j n_j} \cos(m_j\theta - n_j\zeta), \tag{4.4}$$

where j sums over Fourier modes $m_j \leqslant m_{\max}$ and $|n_j| \leqslant n_{\max}$ such that n_j is an integer multiple of N_P, the number of field periods. In (4.4), we have assumed stellarator symmetry such that $B(-\theta, -\zeta) = B(\theta, \zeta)$, and N_p symmetry such that $B(\theta, \zeta + 2\pi/N_P) = B(\theta, \zeta)$. Thus we compute derivatives with respect to the parameters $\Omega = \{B^c_{mn}, I(\psi), G(\psi), \iota(\psi)\}$. Additionally, derivatives with respect to E_r are computed, which are used for efficient ambipolar solutions and computing derivatives of geometric quantities at ambipolarity (see § 5.3) rather than at fixed E_r.

To demonstrate, we compute $\partial\mathcal{R}/\partial B^c_{00}$ for moments of the ion distribution function using the discrete and continuous adjoint methods. A 3-mode model of the standard configuration W7-X geometry at $\rho = \sqrt{\psi/\psi_0} = 0.5$ is used (table 1 in Beidler *et al.* (2011)),

$$B = B^c_{00} + B^c_{01}\cos(N_P\zeta) + B^c_{11}\cos(\theta - N_P\zeta) + B^c_{10}\cos(\theta), \tag{4.5}$$

where $B^c_{01} = 0.04645B^c_{00}$, $B^c_{11} = -0.04351B^c_{00}$ and $B^c_{10} = -0.01902B^c_{00}$. Electron and ion ($Z = 1$) species are included, and the derivatives are computed at the ambipolar E_r with the full trajectory model. The derivatives are also computed with a forward difference approach with varying step size ΔB^c_{00}. In figure 1 we show the fractional difference between $\partial\mathcal{R}/\partial B^c_{00}$ computed using the adjoint method and with forward difference derivatives. We see that at large values of ΔB^c_{00}, the adjoint and numerical derivatives

https://doi.org/10.1017/S0022377819000527 Published online by Cambridge University Press

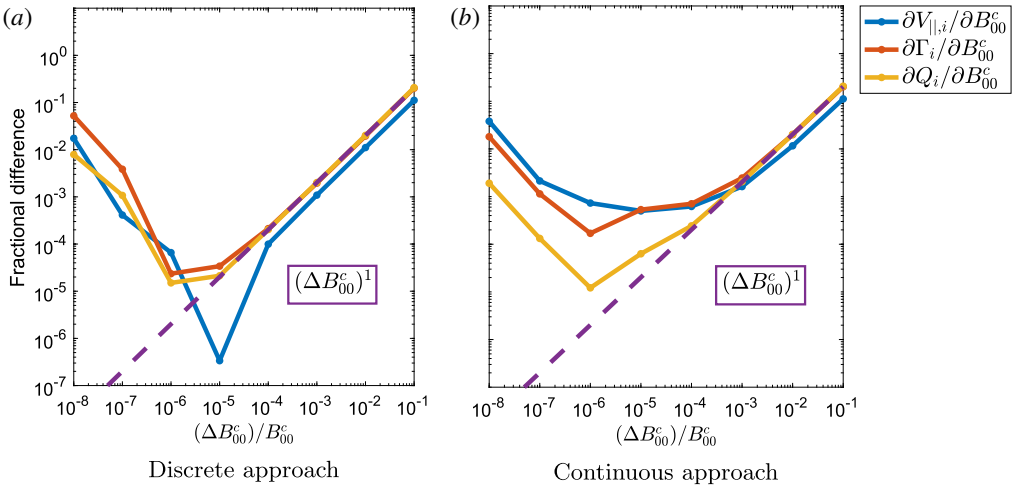


FIGURE 1. Fractional difference between derivatives with respect to B^c_{00} computed with the adjoint method and with a forward difference derivative with step size ΔB^c_{00}. The full trajectory model was used with (*a*) the discrete and (*b*) the continuous adjoint approaches.

begin to differ significantly due to discretization error from the forward difference approximation. The fractional error decreases proportional to ΔB^c_{00} as expected until the rounding error begins to dominate (Sauer 2012) when $\Delta B^c_{00}/(B^c_{00})$ is approximately 10^{-4}, where B^c_{00} is the value of the unperturbed mode. The discrete and continuous approaches show qualitatively similar trends, though the minimum fractional difference is lower in the discrete approach due to the additional discretization error that arises with the continuous approach. With sufficient resolution parameters (41 θ grid points, 61 ζ grid points, 85 ξ basis functions and 7 x basis functions), the fractional error of the continuous approach is $\leqslant 0.1\,\%$ and should not be significant for most applications. We find similar agreement for other derivatives and with the DKES trajectory model.

To demonstrate that the discrete and continuous methods indeed produce the same derivative information, we compute the fractional difference between the derivatives computed with the two methods as a function of the resolution parameters. As an example, in figure 2(*a*) we show the fractional difference in $\partial Q_i/\partial \iota$, where Q_i is the radial ion heat flux, as a function of the number of Legendre polynomials used for the pitch angle discretization, N_ξ, keeping the other resolution parameters fixed. As N_ξ is increased, the fractional differences converges to a finite value, approximately 10^{-4}, due to the discretization error in the other resolution parameters. Similar resolution parameters are required for the convergence of the moment itself, Q_i, and its derivative computed with the continuous method, $\partial Q_i/\partial \iota$. Convergence of Q_i within 5 % is obtained with $N_\xi = 38$, similar to that required for the convergence of $\partial Q/\partial \iota$, as can be seen in figure 2(*a*).

In figure 2(*b*) we compare the cost of calculating derivatives of one moment with respect to N_Ω parameters using the continuous and discrete adjoint methods and forward difference derivatives. All computations are performed on the Edison computer at NERSC using 48 processors, and the elapsed wall time is reported. Here we include the cost of solving the linear system and computing diagnostics $N_\Omega + 1$ times for the forward difference approach, and the cost of solving the forward and adjoint linear systems and computing diagnostics for the adjoint approaches. The cost

https://doi.org/10.1017/S0022377819000527 Published online by Cambridge University Press

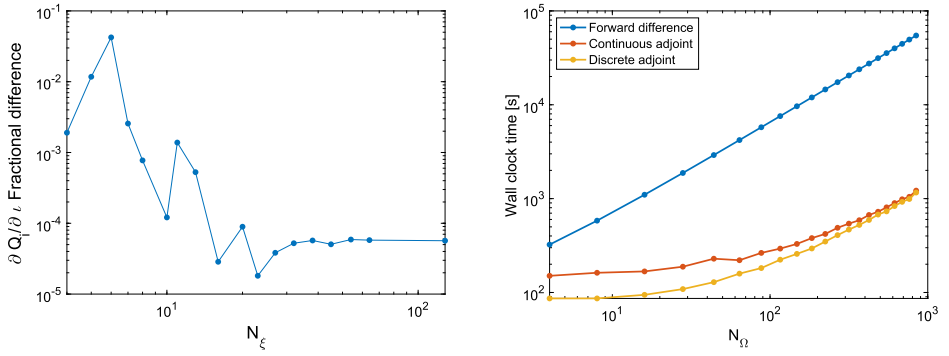


FIGURE 2. (*a*) The fractional difference between $\partial Q_i/\partial \iota$ computed with the continuous and discrete approaches converges with the number of pitch-angle Legendre modes, N_ξ. (*b*) Comparison of the computational cost of computing $\partial \mathcal{R}/\partial \Omega$ with forward difference derivatives and the adjoint approach as a function of N_Ω, the number of parameters in the gradient.

of the continuous approach is slightly more than that of the discrete approach due to the cost of factorizing the adjoint preconditioner. However, at large N_Ω the cost of computing diagnostics for the adjoint approach (e.g. computing $\partial \mathbb{S}/\partial \Omega$ and $\partial \mathbb{L}/\partial \Omega$ and performing the inner product in (3.10)) dominates that of solving the adjoint linear system; thus the discrete and continuous approaches become comparable in cost. In this regime, the adjoint approach provides speed-up by a factor of approximately 50.

5. Applications of the adjoint method

5.1. *Local magnetic sensitivity analysis*

Using the adjoint method, it is possible to compute derivatives of a moment of the distribution function with respect to the Fourier amplitudes of the field strength, $\{\partial \mathcal{R}/\partial B^c_{mn}\}$. Rather than consider sensitivity in Fourier space, we would like to compute the sensitivity to local perturbations of the field strength. We now quantify the relationship between these two representations of sensitivity information.

Consider the Gâteaux functional derivative (Delfour & Zolâsio 2011) of $\mathcal{R}$ with respect to B,

$$\delta \mathcal{R}(\delta B;\, B(\boldsymbol{r})) = \lim_{\epsilon \to 0} \frac{\mathcal{R}(B(\boldsymbol{r}) + \epsilon \delta B(\boldsymbol{r})) - \mathcal{R}(B(\boldsymbol{r}))}{\epsilon}. \tag{5.1}$$

Here we consider a perturbation to the field strength at fixed $I(\psi)$, $G(\psi)$ and $\iota(\psi)$. As $\delta \mathcal{R}(\delta B; B(\boldsymbol{r}))$ is a linear functional of δB, by the Riesz representation theorem (Rudin 2006), $\delta \mathcal{R}$ can be expressed as an inner product with δB and some element of the appropriate space. The function δB is defined on a flux surface, ψ; thus it is sensible to express $\delta \mathcal{R}$ in the following way,

$$\delta \mathcal{R}(\delta B;\, B(\boldsymbol{r})) = \langle S_{\mathcal{R}} \delta B(\boldsymbol{r}) \rangle_\psi. \tag{5.2}$$

Here $\delta B(\boldsymbol{r})$ describes the local perturbation to the field strength, and $\delta \mathcal{R}$ quantifies the corresponding change to the moment $\mathcal{R}$. The function $S_{\mathcal{R}}$ is analogous to the shape gradient, which quantifies the change in a figure of merit which results from

https://doi.org/10.1017/S0022377819000527 Published online by Cambridge University Press

a differential perturbation to a shape (Landreman & Paul 2018). The shape gradient will be discussed further in § 5.2.2.

Suppose that B is stellarator symmetric and N_P symmetric. If $E_r = 0$, then $S_{\mathcal{R}}$ must also possess stellarator and N_P symmetry (see appendix D). However, when $E_r \neq 0$, $S_{\mathcal{R}}$ is no longer guaranteed to have stellarator symmetry. Nonetheless, it may be desirable to ignore the stellarator-asymmetric part of $S_{\mathcal{R}}$ if an optimized stellarator-symmetric configuration is desired. For the remainder of this work, we will make this assumption, though the analysis could be extended to consider the effect of breaking of stellarator symmetry. The quantity $S_{\mathcal{R}}$ can be approximated by a truncated Fourier series under these assumptions,

$$S_{\mathcal{R}} = \sum_k S_{m_k n_k} \cos(m_k\theta - n_k\zeta), \tag{5.3}$$

where k sums over $m \leqslant m_{\max}$ and $|n| \leqslant n_{\max}$ such that n is an integer multiple of N_P. The quantity $\delta B(\boldsymbol{r})$ can be written in terms of perturbations to the Fourier coefficients,

$$\delta B(\boldsymbol{r}) = \sum_j \delta B^c_{m_j n_j} \cos(m_j\theta - n_j\zeta), \tag{5.4}$$

where again the sum is only taken over N_P symmetric modes. Now $\delta\mathcal{R}$ can be written in terms of perturbations to the Fourier coefficients,

$$\delta\mathcal{R} = \sum_j \frac{\partial\mathcal{R}}{\partial B^c_{m_j n_j}} \delta B^c_{m_j n_j}. \tag{5.5}$$

In this way, (5.2) can be expressed as a linear system,

$$\frac{\partial\mathcal{R}}{\partial B^c_{m_j n_j}} = \sum_k D_{jk} S_{m_k n_k}, \tag{5.6}$$

where

$$D_{jk} = V'(\psi)^{-1} \int_0^{2\pi} \mathrm{d}\theta \int_0^{2\pi} \mathrm{d}\zeta \sqrt{g} \cos(m_j\theta - n_j\zeta) \cos(m_k\theta - n_k\zeta). \tag{5.7}$$

If the same number of modes is used to discretize $\delta\mathcal{R}$ and $S_{\mathcal{R}}$, then the linear system is square.

In contrast to derivatives with respect to the Fourier modes of B, the sensitivity function, $S_{\mathcal{R}}$, is a spatially local quantity, quantifying the change in a figure of merit resulting from a local perturbation of the field strength. In this way, $S_{\mathcal{R}}$ can inform where perturbations to the magnetic field strength can be tolerated. The sensitivity function could be related directly to a local magnetic tolerance using the method described in section 9 of Landreman & Paul (2018). In contrast with that work, here we are considering perturbations to the field strength on any flux surface rather than at the plasma boundary. However, $S_{\mathcal{R}}$ still provides insight into where trim coils should be placed or coil displacements can be tolerated without sacrificing desired neoclassical properties. The sensitivity function can also be used for gradient-based optimization in the space of the field strength on a flux surface as in § 5.2.1.

We compute S_{J_b} for the W7-X standard configuration at $\rho = 0.70$, shown in figure 3(*a*). We use a fixed-boundary equilibrium that preceded the coil design and

https://doi.org/10.1017/S0022377819000527 Published online by Cambridge University Press

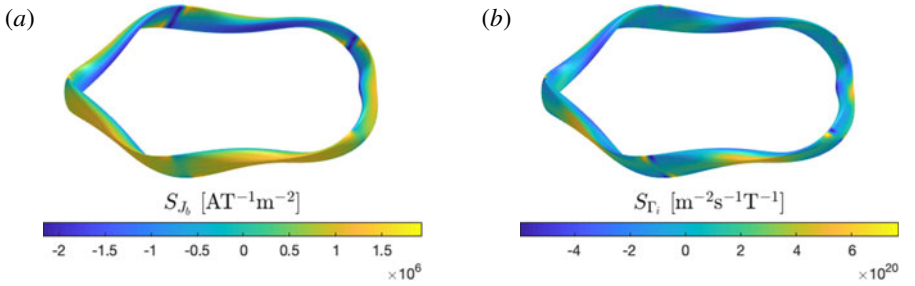


FIGURE 3. (*a*) The local magnetic sensitivity function for the bootstrap current, S_{J_b}, is shown for the W7-X standard configuration. Positive values indicate that increasing the field strength at a given location will increase J_b through (5.2). (*b*) The local sensitivity function for the ion particle flux, S_{Γ_i}.

does not include coil ripple, and the full equilibrium is used rather than the truncated Fourier series considered in § 4. The same resolution parameters are used as in § 4, and derivatives with respect to B^c_{mn} are computed for $m_{\max} = n_{\max} = 20$. The largest modes for this configuration are the helical curvature B^c_{11}, the toroidal curvature B^c_{10} and the toroidal mirror B^c_{01}. We find that S_{J_b} is large and negative on the inboard side, indicating that increasing the magnitude of the toroidal curvature component of B would lead to an increase in J_b. This result is in agreement with previous analysis of the dependence of the bootstrap current on these three modes in the W7-X magnetic configuration space (Maassberg, Lotz & Nührenberg 1993), which found that at low collisionality the bootstrap current coefficients depend strongly on the toroidal curvature. In figure 3(*b*) is the sensitivity function for the ion particle flux, S_{Γ_i}, computed for the same configuration using $m_{\max} = 20$ and $n_{\max} = 25$. We find that the particle flux is more sensitive to perturbations on the outboard side in localized regions, while on the inboard side the sensitivity is relatively small in magnitude.

5.2. *Gradient-based optimization*

5.2.1. *Optimization of field strength*

As a second demonstration of the adjoint neoclassical method, we consider optimizing in the space of the field strength on a surface, taking $\Omega = \{B^c_{mn}\}$. As Boozer coordinates are used, the covariant form (4.1) satisfies $(\nabla \times \boldsymbol{B}) \cdot \nabla \psi = 0$ and the contravariant form (4.2) satisfies $\nabla \cdot \boldsymbol{B} = 0$. As we will artificially modify the field strength while keeping other geometry parameters fixed, the resulting field will not necessarily satisfy both of these conditions with both the covariant and contravariant forms. While there is no guarantee that the resulting field strength will be consistent with a global equilibrium solution, it provides insight into how local changes to the field strength can impact neoclassical properties. As a second step, the outer boundary could be optimized to match the desired field strength on a single surface. In § 5.2.2, we discuss how the derivatives computed in this work could be coupled to optimization of an MHD equilibrium.

We perform optimization with a Broyden–Fletcher–Goldfarb–Shanno (BFGS) quasi-Newton method (Nocedal & Wright 1999) using an objective function $\chi^2 = J_b^2$. A backtracking line search is used at each iteration to find a step size that satisfies a condition of sufficient decrease of χ^2. We use the same equilibrium as in § 5.1,

https://doi.org/10.1017/S0022377819000527 Published online by Cambridge University Press

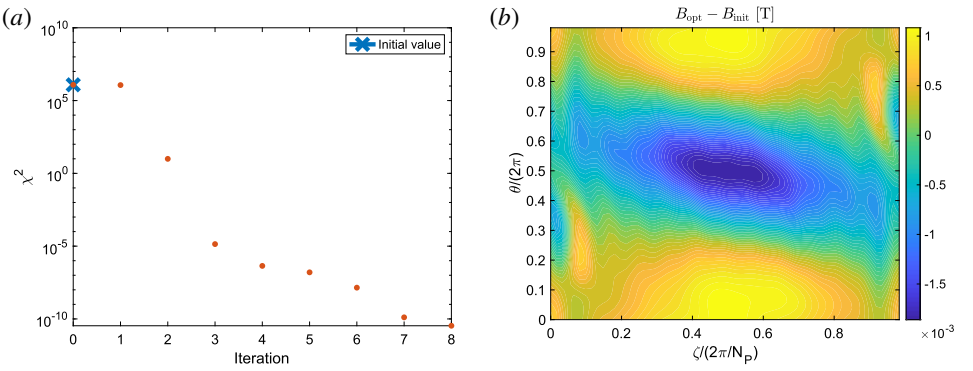


FIGURE 4. (*a*) Convergence of $\chi^2 = J_b^2$ for optimization over $\Omega = \{B^c_{mn}\}$ with an adjoint-based BFGS method. (*b*) The change in field strength from the initial to optimized configuration.

retaining modes $m \leqslant 12$ and $|n| \leqslant 12$, and compute derivatives with respect to these modes. Convergence to $\chi^2 \leqslant 10^{-10}$ was obtained within 8 BFGS iterations (28 function evaluations), as shown in figure 4(*a*). The difference in field strength between the initial and optimized configuration, $B_{\rm opt} - B_{\rm init}$, is shown in figure 4(*b*). As expected from the analysis in § 5.1, the field strength increased on the outboard side and decreased on the inboard side in comparison with $B_{\rm init}$.

5.2.2. *Optimization of MHD equilibria*

The local sensitivity function, $S_{\mathcal{R}}$, along with $\partial\mathcal{R}/\partial I$, $\partial\mathcal{R}/\partial G$, and $\partial\mathcal{R}/\partial\iota$, can be used to determine how perturbations to the outer boundary of the plasma, $\partial\Gamma$, result in perturbations to $\mathcal{R}$. This is quantified through the idea of the shape gradient, which is described below. The partial derivatives of $\mathcal{R}$ can be computed with the adjoint method outlined in § 3, and the shape gradient can be obtained with only one additional MHD equilibrium solution through the application of another adjoint method.

Consider a figure of merit which is integrated over a toroidal domain, Γ,

$$f_{\mathcal{R}}(\Gamma) = \int_{\Gamma} \mathrm{d}^3x\, w(\psi)\mathcal{R}(\psi), \tag{5.8}$$

where $w(\psi)$ is a weighting function. That is, SFINCS is run on a set of ψ surfaces within Γ and the volume integral is computed numerically. Here we consider $\partial\Gamma$ to be the plasma boundary used for a fixed-boundary MHD equilibrium calculation. The perturbation to $f_{\mathcal{R}}$ resulting from normal perturbation to $\partial\Gamma$ can be written in the following form,

$$\delta f_{\mathcal{R}}(\Gamma; \delta\boldsymbol{r}) = \int_{\partial\Gamma} \mathrm{d}^3x\, (\delta\boldsymbol{r}\cdot\boldsymbol{n})\mathcal{G}, \tag{5.9}$$

under certain assumptions of smoothness (Delfour & Zolésio 2011). This can be thought of as another instance of the Riesz representation theorem, as $\delta f_{\mathcal{R}}$ is a linear functional of $\delta\boldsymbol{r}$. Here $\boldsymbol{n}$ is the outward unit normal on $\partial\Gamma$ and $\delta\boldsymbol{r}$ is a vector field describing the perturbation to the surface. Intuitively, only normal perturbations to $\partial\Gamma$

https://doi.org/10.1017/S0022377819000527 Published online by Cambridge University Press

result in a change to $f_{\mathcal{R}}$. The shape gradient is $\mathcal{G}$, which quantifies the contribution of a local normal perturbation of the boundary to the change in $f_{\mathcal{R}}$. The shape gradient can be used for fixed-boundary optimization of equilibria or for analysis of sensitivity to perturbations of magnetic surfaces. It can be computed using a second adjoint method, where a perturbed MHD force balance equation is solved with the addition of a bulk force which depends on derivatives computed from the neoclassical adjoint method (Antonsen *et al.* 2019). While the continuous neoclassical adjoint method described in this work arises from the self-adjointness of the linearized Fokker–Planck operator, the adjoint method for MHD equilibria arises from the self-adjointness of the MHD force operator. In practice these two adjoint methods could be coupled by first computing an MHD equilibrium solution, computing neoclassical transport and its geometric derivatives from this equilibrium with the neoclassical adjoint method, and passing these derivatives back to the equilibrium code to compute the shape gradient with the perturbed MHD adjoint method. In this way derivatives of neoclassical quantities with respect to the shape of the outer boundary are computed with only two equilibrium solutions and two DKE solutions. This calculation will be reported in a future publication.

Rather than solve an additional adjoint equation, the outer boundary could be optimized by numerically computing derivatives of $\{B^c_{mn}(\psi), G(\psi), I(\psi)\}$ with respect to the double Fourier series describing the outer boundary shape in cylindrical coordinates, $\{R^c_{mn}, Z^s_{mn}\}$, using a finite difference method. This could be done using the STELLOPT code (Spong *et al.* 1998; Reiman *et al.* 1999) with BOOZ_XFORM (Sanchez *et al.* 2000) to perform the coordinate transformation. For example, if the rotational transform is held fixed in the variational moments equilibrium code (VMEC) equilibrium calculation (Hirshman & Whitson 1983), the derivative of a moment, $\mathcal{R}$, with respect to a boundary coefficient, R^c_{mn}, can be computed as,

$$\frac{\partial \mathcal{R}(\psi)}{\partial R^c_{mn}} = \sum_{m'n'} \frac{\partial \mathcal{R}(\psi)}{\partial B^c_{m'n'}(\psi)} \frac{\partial B^c_{m'n'}(\psi)}{\partial R^c_{mn}} + \frac{\partial \mathcal{R}(\psi)}{\partial G(\psi)} \frac{\partial G(\psi)}{\partial R^c_{mn}} + \frac{\partial \mathcal{R}(\psi)}{\partial I(\psi)} \frac{\partial I(\psi)}{\partial R^c_{mn}}, \tag{5.10}$$

where $\partial \mathcal{R}(\psi)/\partial B^c_{mn}(\psi)$, $\partial \mathcal{R}(\psi)/\partial G(\psi)$ and $\partial \mathcal{R}(\psi)/\partial I(\psi)$ are computed with the neoclassical adjoint method and $\partial B^c_{mn}(\psi)/\partial R^c_{mn}$, $\partial G(\psi)/\partial R^c_{mn}$ and $\partial I(\psi)/\partial R^c_{mn}$ are computed with finite difference derivatives using STELLOPT. Similarly, derivatives of $\{B^c_{mn}(\psi), G(\psi), I(\psi)\}$ could be computed with respect to coil parameters using a free-boundary equilibrium solution, allowing for direct optimization of neoclassical quantities with respect to coil shapes. The neoclassical calculation with SFINCS is typically significantly more expensive than the equilibrium calculation (for the geometry discussed in § 5.1 fixed-boundary VMEC took 54 s while SFINCS took 157 s on 4 processors of the NERSC Edison computer). As such, combining adjoint-based with finite difference derivatives can still result in a significant computational savings.

5.3. *Ambipolarity*

As stellarators are not intrinsically ambipolar, the radial electric field is not truly an independent parameter. The ambipolar E_r must be obtained which satisfies the condition $J_r(E_r) = 0$. The application of adjoint-based derivatives for computing the ambipolar solution is discussed in § 5.3.1. An adjoint method to compute derivatives with respect to geometric parameters at fixed ambipolarity is discussed in § 5.3.2.

https://doi.org/10.1017/S0022377819000527 Published online by Cambridge University Press

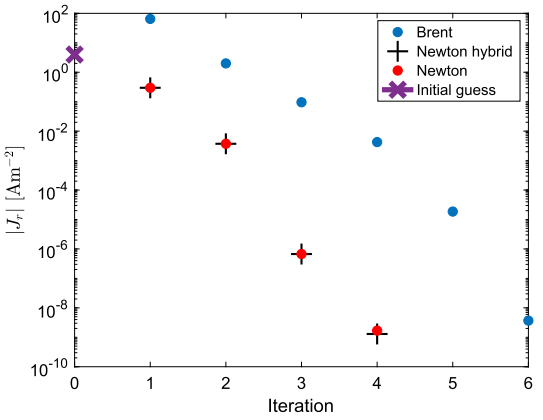


FIGURE 5. The ambipolar root is obtained with Brent, Newton–Raphson and Newton hybrid nonlinear root solvers. The derivatives obtained with the adjoint method provide better convergence properties for the Newton methods.

5.3.1. *Accelerating ambipolar solve*

A nonlinear root-finding algorithm must be used to compute the ambipolar E_r. This root finding can be accelerated with derivative information, such as with a Newton–Raphson method (Press *et al.* 2007). The derivative required, $\partial J_r/\partial E_r$, can be computed with the discrete or continuous adjoint method as described in § 3 with the replacement $\Omega_i \to E_r$, considering $\mathcal{R} = J_r$.

We implement three nonlinear root-finding methods: Brent's method (Brent 2013), the Newton–Raphson method and a hybrid between the bisection and Newton–Raphson methods (Press *et al.* 2007). Brent's method guarantees at least linear convergence by combining quadratic interpolation with bisection and does not require derivatives. The Newton–Raphson method can provide quadratic convergence under certain assumptions but in general is not guaranteed to converge. If an iterate lies near a stationary point or a poor initial guess is given, the method can fail. For this reason we implement the hybrid method, which combines the possible quadratic convergence properties of Newton–Raphson with the guaranteed linear convergence of the bisection method. Both Brent's method and the hybrid method require the root to be bracketed, and therefore may require additional function evaluations in order to obtain the bracket.

We compare these methods in figure 5, using the W7-X standard configuration considered in § 5.1 with the full trajectory model and the discrete adjoint approach, beginning with an initial guess of $E_r = -10$ kV m^{-1} with bounds at $E_r^{\min} = -100$ kV m^{-1} and $E_r^{\max} = 100$ kV m^{-1}. The root is located at $E_r = -3.56$ kV m^{-1}. For this example, the hybrid and Newton methods had nearly identical convergence properties, though the Newton method is less expensive as it does not require J_r to be evaluated at the bounds of the interval. To obtain the same tolerance, the Newton method provided a 14 % savings in wall clock time over Brent's method.

In the above discussion we have made the assumption that there is only one stable root of interest. Of course a given configuration may possess several roots, especially if the ions and electrons are in different collisionality regimes (Hastings, Houlberg & Shaing 1985). Multiple roots can be obtained by performing several root solves with different initial values and brackets, which could be trivially parallelized. Thus the adjoint method could still provide an acceleration in this more general case.

https://doi.org/10.1017/S0022377819000527 Published online by Cambridge University Press

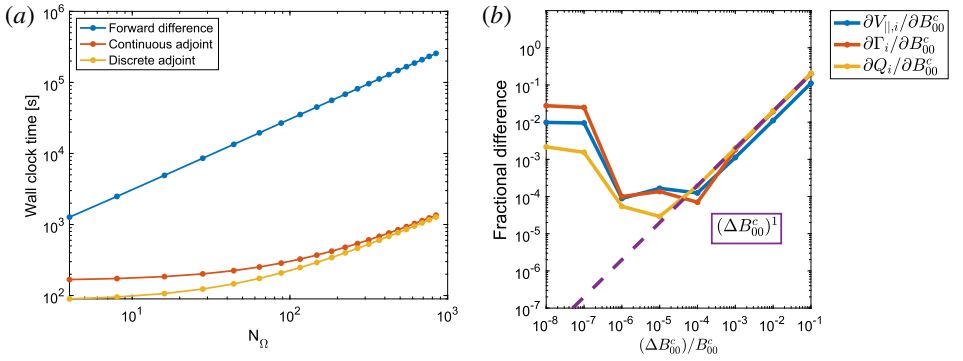


FIGURE 6. (*a*) The cost of computing the gradient $\partial\mathcal{R}/\partial\Omega$ at ambipolarity scales with N_Ω, the number of parameters in Ω. (*b*) The fractional difference between $\partial\mathcal{R}/\partial B^c_{00}$ at constant ambipolarity obtained with the adjoint method and with finite difference derivatives.

5.3.2. *Derivatives at ambipolarity*

The adjoint method described in § 3 assumes that E_r is held constant when computing derivatives with respect to Ω. However, E_r cannot truly be determined independently from geometric quantities, as the ambipolar solution should be recomputed as the geometry is altered. It is therefore desirable to compute derivatives at fixed ambipolarity (fixed $J_r = 0$) rather than at fixed E_r. This is performed by solving an additional adjoint equation,

$$\mathbb{L}^\dagger q^{J_r} = \widetilde{J}_r, \tag{5.11}$$

in the continuous approach or

$$(\overleftrightarrow{\boldsymbol{L}})^{\mathrm{T}}\overrightarrow{\boldsymbol{q}}^{J_r} = \overrightarrow{\boldsymbol{J}}_r, \tag{5.12}$$

in the discrete approach. Details are described in appendix E.

It should be noted that by computing derivatives at ambipolarity we assume that a given moment $\mathcal{R}$ is a differentiable function of the geometry at fixed $J_r = 0$. That is, this method cannot be applied to cases in which a stable root disappears as the geometry varies. As this will occur at a stationary point of $J_r(E_r)$, this situation could be avoided within an optimization loop by computing derivatives at constant E_r rather than constant J_r if $|\partial J_r/\partial E_r|$ falls below a given threshold at ambipolarity.

Although an additional adjoint solve is required, this method of computing derivatives at ambipolarity is advantageous as several linear solves are typically required to obtain the ambipolar root. A comparison of the computational cost between the adjoint method and forward difference method for derivatives at ambipolarity is shown in figure 6(*a*). Here the full trajectory model is used, and the result for both the discrete and continuous adjoint methods are shown. For the finite difference derivative, the ambipolar solve is performed with Brent's method at each step in Ω. As in figure 2(*b*), we find that for large N_Ω the cost of the continuous and discrete approaches are essentially the same, as the cost is no longer dominated by the linear solve. When computing the derivatives at ambipolarity, both adjoint methods decrease the cost by a factor of approximately 200 for large N_Ω.

https://doi.org/10.1017/S0022377819000527 Published online by Cambridge University Press

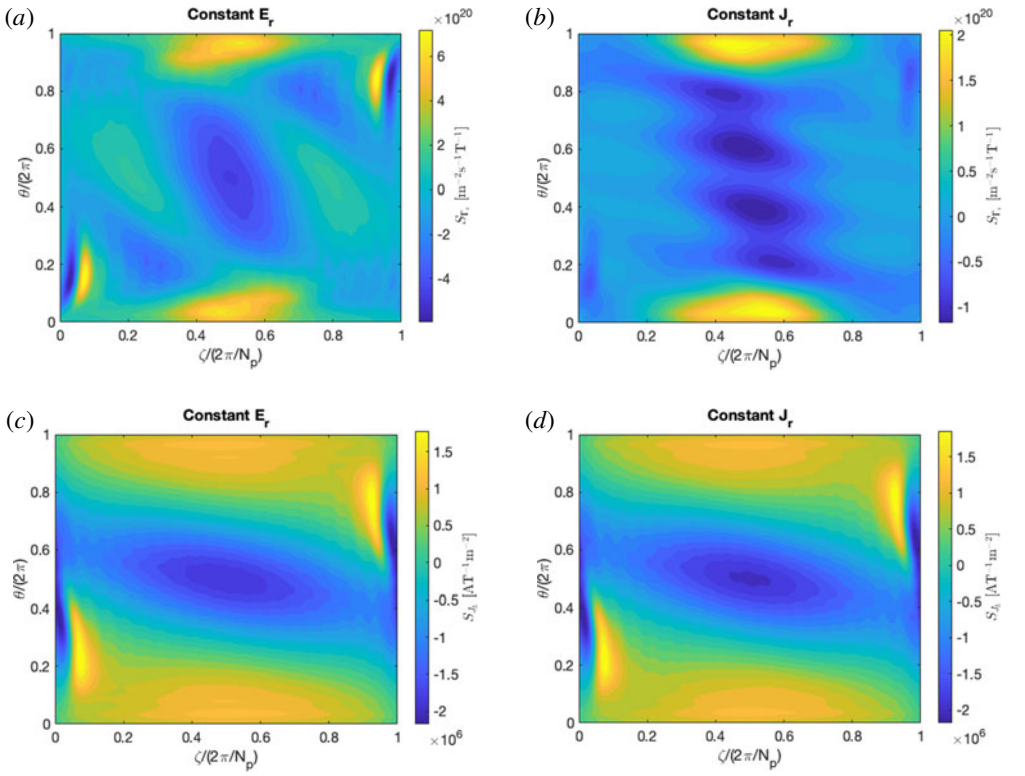


FIGURE 7. The sensitivity function for the ion particle flux, S_{Γ_i}, is computed at (*a*) constant E_r and (*b*) constant J_r. Similarly, S_{J_b} is computed at (*c*) constant E_r and (*d*) constant J_r.

In figure 6(*b*) we show a benchmark between derivatives at ambipolarity, $(\partial\mathcal{R}/\partial B_{00}^c)_{J_r}$, computed with the discrete adjoint method and with forward difference derivatives. For the forward difference method, the Newton solver is used to obtain the ambipolar E_r as B_{00}^c is varied. As the forward difference step size ΔB_{00}^c decreases, the fractional difference again decreases proportional to ΔB_{00}^c until it reaches a minimum when $\Delta B_{00}^c/B_{00}^c$ is approximately 10^{-4}. In comparison with figure 1, we see that the minimum fractional difference is slightly larger at fixed ambipolarity than at fixed E_r, as the tolerance parameters associated with the Newton solver introduce an additional source of error to the forward difference approach.

In figure 7(*a*,*b*) we compare the sensitivity function for the particle flux, S_{Γ_i}, computed using derivatives at constant E_r with that computed at constant J_r. Here derivatives are computed using the discrete adjoint method with full trajectories, and the sensitivity function is constructed as described in § 5.1. The configuration and numerical parameters are the same as described in § 5.1. At constant J_r the large region of increased sensitivity on the outboard side that appears at constant E_r remains, though the overall magnitude of the sensitivity decreases. Thus it may be important to account for the effect of the ambipolar E_r when optimizing for radial transport. In figure 7(*c*,*d*) we perform the same comparison for S_{J_b}, finding the derivatives at fixed E_r and at fixed J_r to be virtually identical. This is to be expected, as numerical calculations of neoclassical transport coefficients for W7-X have found

https://doi.org/10.1017/S0022377819000527 Published online by Cambridge University Press

that the bootstrap coefficients are much less sensitive to E_r than those for the radial transport (figures 18 and 26 in Beidler *et al.* (2011)). Furthermore, the bootstrap current in the $1/\nu$ regime is independent of E_r, and the finite-collisionality correction is small for optimized stellarators, such as W7-X (Helander, Parra & Newton 2017). Therefore, the ambipolarity corrections to the derivatives are less important for J_b than for the radial transport.

6. Conclusions

We have described a method by which moments $\mathcal{R}$ of the neoclassical distribution function can be differentiated efficiently with respect to many parameters. The adjoint approach requires defining an inner product from which the adjoint operator is obtained. We consider two choices for this inner product. One choice corresponds with computing the adjoint of the linear operator after discretization, and the other corresponds with computing it before discretization. In the case of the former, the Euclidean dot product can be used, and in the case of the latter, an inner product whose corresponding norm is similar to the free energy norm (3.1) is defined. In § 4, we show that these approaches provide the same derivative information within discretization error, as expected. Both methods provide reduction in computational cost by a factor of approximately 50 in comparison with forward difference derivatives when differentiating with respect to many ($O(10^2)$) parameters. In § 5.3.2 the adjoint method is extended to compute derivatives at ambipolarity. This method provides a reduction in cost by a factor of approximately 200 over a forward difference approach. We have implemented this method in the SFINCS code, and similar methods could be applied to other drift kinetic solvers.

In this work we consider derivatives with respect to geometric quantities that enter the DKE through Boozer coordinates. However, the adjoint neoclassical method we have described is much more general, allowing for many possible applications. For example, derivatives of the radial fluxes with respect to the temperature and density profiles could be used to accelerate the solution of the transport equations using a Newton method (Barnes *et al.* 2010). The transport solution could furthermore be incorporated into the optimization loop to self-consistently evolve the macroscopic profiles in the presence of neoclassical fluxes. Rather than simply optimizing for minimal fluxes, an objective function such as the total fusion power could be considered (Highcock *et al.* 2018), with optimization accelerated by adjoint-based derivatives.

Another application of the continuous adjoint formulation is correction of discretization error. The same solution obtained in § 3.1 can be used to quantify and correct for the error in a moment, $\mathcal{R}$, providing similar accuracy to that computed with a higher-order stencil or finer mesh without the associated cost. This method has been applied in the field of computational fluid dynamics by solving adjoint Euler equations (Venditti & Darmofal 1999; Pierce & Giles 2004) and could prove useful for efficiently obtaining solutions of the DKE in low-collisionality regimes.

In § 5.2.1 we have shown an example of adjoint-based neoclassical optimization, where the optimization space is taken to be the Fourier modes of the field strength on a surface, $\{B^c_{mn}\}$. While optimization within this space is not necessarily consistent with a global equilibrium solution, it demonstrates the adjoint neoclassical method for efficient optimization. In § 5.2.2, two approaches to self-consistently optimize MHD equilibria are discussed. Further discussion and demonstration of these approaches will be provided in a future publication.

https://doi.org/10.1017/S0022377819000527 Published online by Cambridge University Press

In appendix D we show that when $E_r = 0$ and the unperturbed geometry is stellarator symmetric, the sensitivity functions for moments of the distribution function are also stellarator symmetric. However, when $E_r \neq 0$ this is no longer true. This implies that obtaining minimal neoclassical transport in the $\sqrt{\nu}$ regime may require breaking of stellarator symmetry. In this work we have ignored the effects of stellarator symmetry breaking, although we hope to extend this work to study these effects in the future.

Acknowledgements

The authors acknowledge helpful discussion with L.-M. Imbert-Gérard and assistance with the STELLOPT code from S. Lazerson. This work was supported by the US Department of Energy through grants DE-FG02-93ER-54197 and DE-FC02-08ER-54964. The computations presented in this paper have used resources at the National Energy Research Scientific Computing Center (NERSC). Support for I.G.A. for the initial work was provided by the Chalmers University of Technology, under the auspices of the Framework grant for Strategic Energy Research (Dnr. 2014-5392) from Vetenskapsråadet.

Appendix A. Trajectory models

In the SFINCS coordinate system, the DKE can be written in the following way,

$$\dot{\boldsymbol{r}} \cdot \nabla f_{1s} + \dot{x}_s \frac{\partial f_{1s}}{\partial x_s} + \dot{\xi}_s \frac{\partial f_{1s}}{\partial \xi_s} - C_s(f_{1s}) = -(\boldsymbol{v}_{\mathrm{ms}} \cdot \nabla \psi) \frac{\partial f_{Ms}}{\partial \psi}. \tag{A 1}$$

To obtain the trajectory coefficients ($\dot{\boldsymbol{r}}$, $\dot{x}_s$ and $\dot{\xi}_s$) several approximations are made. For example, any terms that require radial coupling (ψ derivatives of f_{1s}) cannot be retained, as this would necessitate solving a five-dimensional system.

Under the full trajectory model, the trajectory coefficients are chosen such that μ conservation is maintained as radial coupling is dropped,

$$\left.\begin{aligned} \dot{\boldsymbol{r}} &= v_\parallel \boldsymbol{b} + \frac{1}{B^2}\frac{\mathrm{d}\Phi}{\mathrm{d}\psi}\boldsymbol{B} \times \nabla \psi, \\ \dot{x}_s &= -(\boldsymbol{v}_{\mathrm{ms}} \cdot \nabla \psi)\frac{q_s}{2T_s x_s}\frac{\mathrm{d}\Phi}{\mathrm{d}\psi}, \\ \dot{\xi}_s &= -\frac{1-\xi_s^2}{2B\xi_s} v_\parallel \boldsymbol{b} \cdot \nabla B + \xi_s(1-\xi_s^2)\frac{1}{2B^3}\frac{\mathrm{d}\Phi}{\mathrm{d}\psi}\boldsymbol{B} \times \nabla \psi \cdot \nabla B. \end{aligned}\right\} \tag{A 2}$$

Under the DKES trajectory model, the $\boldsymbol{E} \times \boldsymbol{B}$ velocity is taken to be divergenceless,

$$\boldsymbol{v}_E^{\mathrm{DKES}} = \frac{\boldsymbol{B} \times \nabla \Phi}{\langle B^2 \rangle_\psi}, \tag{A 3}$$

where the flux surface average of a quantity A is,

$$\langle A \rangle_\psi = V'(\psi)^{-1} \int_0^{2\pi} \mathrm{d}\theta \int_0^{2\pi} \mathrm{d}\zeta \sqrt{g} A, \tag{A 4}$$

https://doi.org/10.1017/S0022377819000527 Published online by Cambridge University Press

$\sqrt{g} = (\nabla\psi \times \nabla\theta \cdot \nabla\zeta)^{-1}$ is the Jacobian, and $V'(\psi) = \int_0^{2\pi} \mathrm{d}\theta \int_0^{2\pi} \mathrm{d}\zeta \sqrt{g}$. Under the DKES trajectory model, the trajectory coefficients are taken to be,

$$\left.\begin{aligned} \dot{\boldsymbol{r}} &= v_\parallel \boldsymbol{b} + \frac{1}{\langle B^2\rangle_\psi}\frac{\mathrm{d}\Phi}{\mathrm{d}\psi}\boldsymbol{B}\times\nabla\psi, \\ \dot{x}_s &= 0, \\ \dot{\xi}_s &= -\frac{1-\xi_s^2}{2B\xi_s} v_\parallel \boldsymbol{b}\cdot\nabla B. \end{aligned}\right\} \tag{A 5}$$

These effective trajectories are adopted in the widely used DKES code (Hirshman *et al.* 1986*b*; van Rij & Hirshman 1989).

Appendix B. Adjoint collision operator

We want to find an adjoint collision operator, $C_s^\dagger$, that satisfies the following relation,

$$\left\langle \int \mathrm{d}^3 v \, \frac{g_{1s} C_s(f_{1s})}{f_{Ms}} \right\rangle_\psi = \left\langle \int \mathrm{d}^3 v \, \frac{f_{1s} C_s^\dagger(g_{1s})}{f_{Ms}} \right\rangle_\psi . \tag{B 1}$$

The linearized Fokker–Planck collision operator can be written as

$$C_s(f_{1s}) = \sum_{s'} C^L_{ss'}(f_{1s}, f_{1s'}) = \sum_{s'} C_{ss'}(f_{1s}, f_{Ms'}) + C_{ss'}(f_{Ms}, f_{1s'}), \tag{B 2}$$

where s' sums over species. The first term on the right-hand side of (B 2) is referred to as the test-particle collision operator, $C^{\mathrm{T}}_{ss'}(f_{1s}) = C_{ss'}(f_{1s}, f_{Ms'})$, and the second the field-particle collision operator, $C^F_{ss'}(f_{1s'}) = C_{ss'}(f_{Ms}, f_{1s'})$. The test and field terms satisfy the following relations (Rosenbluth, Hazeltine & Hinton 1972; Sugama, Watanabe & Nunami 2009),

$$\int \mathrm{d}^3 v \, \frac{g_{1s} C_{ss'}(f_{1s}, f_{Ms'})}{f_{Ms}} = \int \mathrm{d}^3 v \, \frac{f_{1s} C_{ss'}(g_{1s}, f_{Ms'})}{f_{Ms}}, \tag{B 3}$$

$$\int \mathrm{d}^3 v \, \frac{g_{1s} C_{ss'}(f_{Ms}, f_{1s'})}{f_{Ms}} = \frac{T_{s'}}{T_s} \int \mathrm{d}^3 v \, \frac{f_{1s'} C_{s's}(f_{Ms'}, g_{1s})}{f_{Ms'}}. \tag{B 4}$$

For collisions between species of the same temperature, we see that $C_s(f_{1s})$ is self-adjoint. The adjoint operator with respect to the inner product (3.1) is thus,

$$C_s^\dagger = C_s^{\mathrm{T}} + \sum_{s'} \frac{f_{Ms}}{f_{Ms'}} \frac{T_{s'}}{T_s} C^F_{s's}. \tag{B 5}$$

Appendix C. Adjoint collisionless trajectories

We want to find an adjoint operator, $\mathbb{L}_{0s}^\dagger$, that satisfies,

$$\left\langle \int \mathrm{d}^3 v \, \frac{g_{1s} \mathbb{L}_{0s} f_{1s}}{f_{Ms}} \right\rangle_\psi = \left\langle \int \mathrm{d}^3 v \, \frac{f_{1s} \mathbb{L}_{0s}^\dagger g_{1s}}{f_{Ms}} \right\rangle_\psi , \tag{C 1}$$

for both trajectory models, where $\mathbb{L}_{0s}$ is defined in (2.8) with (A 5) for the DKES trajectories model and (A 2) for the full trajectory model. Throughout we use the velocity-space element in SFINCS coordinates, $\mathrm{d}^3 v = 2\pi v_{ts}^3 x_s^2 \, \mathrm{d}\xi_s \, \mathrm{d}x_s$.

https://doi.org/10.1017/S0022377819000527 Published online by Cambridge University Press

C.1. *DKES trajectories*

The operator under consideration is,

$$\mathbb{L}_{0s} = v_\parallel \boldsymbol{b}\cdot\nabla + \boldsymbol{v}_E^{\mathrm{DKES}}\cdot\nabla - \frac{1-\xi_s^2}{2B\xi_s} v_\parallel \boldsymbol{b}\cdot\nabla B\frac{\partial}{\partial\xi_s}. \tag{C 2}$$

Considering the contribution of the streaming term in (C 2) to the left-hand side of (C 1) we obtain,

$$\left\langle \int \mathrm{d}^3v\, \frac{g_{1s} v_\parallel \boldsymbol{b}\cdot\nabla f_{1s}}{f_{Ms}} \right\rangle_\psi = -\left\langle \int \mathrm{d}^3v\, \frac{f_{1s} v_\parallel \boldsymbol{B}\cdot\nabla(g_{1s}/B)}{f_{Ms}} \right\rangle_\psi. \tag{C 3}$$

Here the identity $\langle\nabla\cdot\boldsymbol{Q}\rangle_\psi = 1/V'(\psi)\partial/\partial\psi(V'(\psi)\langle\boldsymbol{Q}\cdot\nabla\psi\rangle_\psi)$ for any vector $\boldsymbol{Q}$ has been used. We next consider the contribution of the $\boldsymbol{E}\times\boldsymbol{B}$ drift term in (C 2),

$$\left\langle \int \mathrm{d}^3v\, \frac{g_{1s}\boldsymbol{v}_E^{\mathrm{DKES}}\cdot\nabla f_{1s}}{f_{Ms}} \right\rangle_\psi = -\left\langle \int \mathrm{d}^3v\, \frac{f_{1s}\boldsymbol{v}_E^{\mathrm{DKES}}\cdot\nabla g_{1s}}{f_{Ms}} \right\rangle_\psi. \tag{C 4}$$

Here we have used the identity

$$\langle \boldsymbol{B}\times\nabla\psi\cdot\nabla w\rangle_\psi = 0, \tag{C 5}$$

for any w. We consider the contribution of the mirror-force term in (C 2),

$$\left\langle \int \mathrm{d}^3v\, \frac{g_{1s}\dot{\xi}_s}{f_{Ms}}\frac{\partial f_{1s}}{\partial\xi_s} \right\rangle_\psi = -\left\langle \int \mathrm{d}^3v\, \frac{f_{1s}\dot{\xi}_s}{f_{Ms}}\frac{\partial g_{1s}}{\partial\xi_s} \right\rangle_\psi - \left\langle \int \mathrm{d}^3v\, \frac{v_\parallel}{B}\boldsymbol{b}\cdot\nabla B\frac{g_{1s}f_{1s}}{f_{Ms}} \right\rangle_\psi. \tag{C 6}$$

Combining (C 3)–(C 6), we obtain

$$\left\langle \int \mathrm{d}^3v\, \frac{g_{1s}\mathbb{L}_{0s}f_{1s}}{f_{Ms}} \right\rangle_\psi = -\left\langle \int \mathrm{d}^3v\, \frac{f_{1s}\mathbb{L}_{0s}g_{1s}}{f_{Ms}} \right\rangle_\psi. \tag{C 7}$$

Therefore, in the DKES trajectory model we obtain (3.13).

C.2. *Full trajectories*

The operator under consideration for the full model is,

$$\begin{aligned}\mathbb{L}_{0s} \;=\; & v_\parallel \boldsymbol{b}\cdot\nabla + \boldsymbol{v}_E\cdot\nabla + \frac{(1+\xi_s^2)x_s}{2B}\boldsymbol{v}_E\cdot\nabla B\frac{\partial}{\partial x_s} \\ & - \frac{1-\xi_s^2}{2B\xi_s} v_\parallel \boldsymbol{b}\cdot\nabla B\frac{\partial}{\partial\xi_s} + \frac{\xi_s(1-\xi_s^2)}{2B}\boldsymbol{v}_E\cdot\nabla B\frac{\partial}{\partial\xi_s}.\end{aligned} \tag{C 8}$$

The contribution to (C 1) from the streaming term in (C 8) is identical to that in the case of the DKES trajectory model, (C 3). We next consider the contribution from the $\boldsymbol{E}\times\boldsymbol{B}$ drift term in (C 8),

$$\left\langle \int \mathrm{d}^3v\, \frac{g_{1s}\boldsymbol{v}_E\cdot\nabla f_{1s}}{f_{Ms}} \right\rangle_\psi = -\left\langle \int \mathrm{d}^3v\, \frac{f_{1s}B^2\boldsymbol{v}_E\cdot\nabla(g_{1s}/B^2)}{f_{Ms}} \right\rangle_\psi, \tag{C 9}$$

https://doi.org/10.1017/S0022377819000527 Published online by Cambridge University Press

again using (C 5). The contribution from the $\dot{x}_s$ term in (C 8) is,

$$\left\langle \int \mathrm{d}^3 v \, \frac{g_{1s}\dot{x}_s}{f_{Ms}} \frac{\partial f_{1s}}{\partial x_s} \right\rangle_\psi = -\left\langle \int \mathrm{d}^3 v \, \frac{f_{1s}\dot{x}_s}{f_{Ms}} \frac{\partial g_{1s}}{\partial x_s} \right\rangle_\psi - \left\langle \int \mathrm{d}^3 v \, (3+2x_s^2)(1+\xi_s^2) \frac{g_{1s} f_{1s}}{2 f_{Ms} B} \boldsymbol{v}_E \cdot \nabla B \right\rangle_\psi . \tag{C 10}$$

The contribution from the mirror term in (C 8) is the same as in the case of the DKES trajectories model (C 6). We consider the contribution from the final term in (C 8),

$$\left\langle \int \mathrm{d}^3 v \frac{g_{1s}\xi_s(1-\xi_s^2)\boldsymbol{v}_E \cdot \nabla B}{2Bf_{Ms}} \frac{\partial f_{1s}}{\partial \xi_s} \right\rangle_\psi = -\left\langle \int \mathrm{d}^3 v \frac{f_{1s}\xi_s(1-\xi_s^2)\boldsymbol{v}_E \cdot \nabla B}{2Bf_{Ms}} \frac{\partial g_{1s}}{\partial \xi_s} \right\rangle_\psi - \left\langle \int \mathrm{d}^3 v \, (1-3\xi_s^2)\boldsymbol{v}_E \cdot \nabla B \frac{f_{1s} g_{1s}}{2Bf_M} \right\rangle_\psi . \tag{C 11}$$

Combining (C 3), (C 9), (C 10), (C 6) and (C 11), we obtain

$$\left\langle \int \mathrm{d}^3 v \, \frac{g_{1s}\mathbb{L}_{0s} f_{1s}}{f_{Ms}} \right\rangle_\psi = -\left\langle \int \mathrm{d}^3 v \frac{f_{1s}\mathbb{L}_{0s} g_{1s}}{f_{Ms}} \right\rangle_\psi + \frac{\mathrm{d}\Phi}{\mathrm{d}\psi} \frac{q_s}{T_s} \left\langle \int \mathrm{d}^3 v \, (\boldsymbol{v}_{\mathrm{ms}} \cdot \nabla \psi) \frac{f_{1s} g_{1s}}{f_{Ms}} \right\rangle_\psi . \tag{C 12}$$

Therefore, under the full trajectory model we obtain (3.14).

Appendix D. Symmetry of the sensitivity function

In this appendix we discuss several symmetry properties of the local sensitivity function, $S_\mathcal{R}$, defined through (5.2). The arguments that follow are similar to those in appendix C of Landreman & Paul (2018). Throughout we will assume that B is stellarator symmetric and N_P symmetric. We will show that this implies N_P symmetry of $S_\mathcal{R}$. In the limit that $E_r \to 0$, then $S_\mathcal{R}$ also has stellarator symmetry.

D.1. *Symmetry of $S_\mathcal{R}$ implied by Fourier derivatives*

First we would like to show that $S_\mathcal{R}$ is stellarator symmetric if and only if $\partial\mathcal{R}/\partial B^s_{mn} = 0$ for all m and n, where we express B in a Fourier series,

$$B = \sum_j B^c_{m_j n_j} \cos(m_j\theta - n_j\zeta) + B^s_{m_j n_j} \sin(m_j\theta - n_j\zeta). \tag{D 1}$$

The perturbation, δB, is decomposed similarly. We begin with the 'if' portion of the argument. From (5.2) we have,

$$\frac{\partial \mathcal{R}}{\partial B^s_{mn}} = V'(\psi)^{-1} \int_0^{2\pi} \mathrm{d}\theta \int_0^{2\pi} \mathrm{d}\zeta \sqrt{g} S_\mathcal{R} \sin(m\theta - n\zeta). \tag{D 2}$$

Suppose $\partial\mathcal{R}/\partial B^s_{mn} = 0$ for all m and n. The quantity $(\sqrt{g}S_\mathcal{R})$ can be represented as a Fourier series,

$$(\sqrt{g}S_\mathcal{R}) = \sum_j A^c_{m_j n_j} \cos(m_j\theta - n_j\zeta) + A^s_{m_j n_j} \sin(m_j\theta - n_j\zeta). \tag{D 3}$$

https://doi.org/10.1017/S0022377819000527 Published online by Cambridge University Press

From (D 2), we see that $A^s_{mn} = 0$ for all m and m. Thus the quantity $(\sqrt{g}S_{\mathcal{R}})$ must be even under the transformation $(\theta, \zeta) \to (-\theta, -\zeta)$. We now note that $\sqrt{g}$ must be even from (4.3) under the assumption that B is stellarator symmetric. Therefore $S_{\mathcal{R}}$ must be stellarator symmetric, assuming that $\sqrt{g}$ does not vanish anywhere, which must be the case for any well-defined coordinate transformation.

We continue with the 'only if' portion of the argument. Suppose $S_{\mathcal{R}}$ is stellarator symmetric. As $\sqrt{g}$ is also stellarator symmetric, $(\sqrt{g}S_{\mathcal{R}})$ can be expressed in a Fourier series as (D 3) with $A^s_{mn} = 0$ for all m and n. Thus from (D 2) $\partial\mathcal{R}/\partial B^s_{mn} = 0$ for all m and n.

We next show that if B is N_P symmetric, then $S_{\mathcal{R}}$ is N_P symmetric if and only if $\partial\mathcal{R}/\partial B^c_{mn} = 0$ for all n that are not integer multiples of N_P. We begin with the 'if' portion of the argument. From (5.2),

$$\frac{\partial \mathcal{R}}{\partial B^c_{mn}} = V'(\psi)^{-1} \int_0^{2\pi} \mathrm{d}\theta \int_0^{2\pi} \mathrm{d}\zeta \sqrt{g} S_{\mathcal{R}} \cos(m\theta - n\zeta). \tag{D 4}$$

Suppose $\partial\mathcal{R}/\partial B^c_{mn} = 0$ for all n which are not integer multiples of N_P. Here $(\sqrt{g}S_{\mathcal{R}})$ can be expressed in a Fourier series as (D 3) with $A^s_{mn} = 0$ for all m and n. Inserting the Fourier series into (D 4), we find that $A^c_{mn} = 0$ for all n that are not integer multiples of N_P. Thus $(\sqrt{g}S_{\mathcal{R}})$ must be N_P symmetric. As $\sqrt{g}$ must be N_P symmetric, this implies $S_{\mathcal{R}}$ possesses the same symmetry.

Next we consider the 'only if' portion of the argument. Suppose that $S_{\mathcal{R}}$ is N_P symmetric. As $\sqrt{g}$ is also N_P symmetric, then $(\sqrt{g}S_{\mathcal{R}})$ can be expressed in a Fourier series as (D 3) where the sum includes n that are integer multiples of N_P. Inserting the Fourier series into (D 4), we find that $\partial\mathcal{R}/\partial B^c_{mn} = 0$ for all n that are not integer multiples of N_P.

D.2. *Symmetry of Fourier derivatives*

To continue, we need to show that $\partial\mathcal{R}/\partial B^s_{mn} = 0$ for all m and n and $\partial\mathcal{R}/\partial B^c_{mn} = 0$ for all n which are not integer multiples of N_P. We begin with the N_P symmetry argument. We consider the symmetry of f_{1s} implied by (A 1). Under the transformation $\zeta \to \zeta + 2\pi/N_P$, we find that each of the trajectory coefficients remain unchanged, as well as the source term and collision operator. Therefore we can conclude that f_{1s} is N_P symmetric. We can also note that each of the $\widetilde{\mathcal{R}}$ vectors are N_P symmetric, as well as $\sqrt{g}$. We consider the integrand that appears in the flux surface average in (3.3),

$$D_s(\theta, \zeta) = \int \mathrm{d}^3 v \frac{f_{1s}\widetilde{\mathcal{R}}^f_s \sqrt{g}}{f_{Ms}}. \tag{D 5}$$

Here the superscript and subscript on $\widetilde{\mathcal{R}}$ denotes that we consider the unknowns corresponding to the distribution function of species s. We note that $D_s(\theta, \zeta + 2\pi/N_P) = D_s(\theta, \zeta)$. The quantity $\mathcal{R}$ can be expressed in terms of D_s as follows,

$$\mathcal{R} = \sum_s V'(\psi)^{-1} \int_0^{2\pi} \mathrm{d}\zeta \int_0^{2\pi} \mathrm{d}\theta\, D_s. \tag{D 6}$$

Next we consider the functional derivative of $\mathcal{R}$ with respect to B, defined as in (5.1). The derivative with respect to B^c_{mn} can be thus defined as,

$$\frac{\partial \mathcal{R}}{\partial B^c_{mn}} = V'(\psi)^{-1} \int_0^{2\pi} \mathrm{d}\zeta \int_0^{2\pi} \mathrm{d}\theta \left(\sum_s \frac{\delta D_s}{\delta B} - \mathcal{R}\frac{\delta \sqrt{g}}{\delta B} \right) \cos(m\theta - n\zeta). \tag{D 7}$$

https://doi.org/10.1017/S0022377819000527 Published online by Cambridge University Press

As the functional derivative maintains the N_P symmetry of D_s and $\sqrt{g}$, the quantity in parenthesis in (D 7) can be expressed in a Fourier series containing only n that are integer multiples of N_P. Thus we see that the quantity $\partial\mathcal{R}/\partial B^c_{mn} = 0$ for all n that are not integer multiples of N_P.

Next we consider a similar argument for stellarator symmetry. We begin by considering the symmetry of f_{1s} implied by (A 1) in the case $E_r = 0$. Under the transformation $(\theta, \zeta, v_\parallel) \to (-\theta, -\zeta, -v_\parallel)$, we see that both the collisionless trajectory operator and the collision operator maintain the parity of f_{1s}, while the source term is odd. Therefore, f_{1s} must be odd under this transformation. In this case, we can write f_{1s} as

$$f_{1s} = f^-_{a,s}(x_s, \xi_s) f^+_{b,s}(\theta, \zeta) + f^+_{a,s}(x_s, \xi_s) f^-_{b,s}(\theta, \zeta), \tag{D 8}$$

where $f^-_{a,s}(x_s, -\xi_s) = -f^-_{a,s}(x_s, \xi_s)$, $f^+_{a,s}(x_s, -\xi_s) = f^+_{a,s}(x_s, -\xi_s)$ and analogous expressions for $f^+_{b,s}$ and $f^-_{b,s}$.

We next note that each of the $\widetilde{\mathcal{R}}^f_s$ are odd under the transformation $(\theta, \zeta, v_\parallel) \to (-\theta, -\zeta, -v_\parallel)$. As $\sqrt{g}$ is even, then we can express $\widetilde{\mathcal{R}}^f_s\sqrt{g}$ in a similar way to (D 8),

$$\widetilde{\mathcal{R}}^f_s\sqrt{g} = B^-_{a,s}(x_s, \xi_s) B^+_{b,s}(\theta, \zeta) + B^+_{a,s}(x_s, \xi_s) B^-_{b,s}(\theta, \zeta). \tag{D 9}$$

The integrand that appears in the flux surface average becomes,

$$\begin{aligned} D_s \;=\; & \int \mathrm{d}^3 v f^{-1}_{Ms} \left(f^-_{a,s}(x_s, \xi_s) B^-_{a,s}(x_s, \xi_s) f^+_{b,s}(\theta, \zeta) B^+_{b,s}(\theta, \zeta) \right. \\ & \left. + f^+_{a,s}(x_s, \xi_s) B^+_{a,s}(x_s, \xi_s) f^-_{b,s}(\theta, \zeta) B^-_{b,s}(\theta, \zeta) \right). \end{aligned} \tag{D 10}$$

We see that D_s is even with respect to the transformation $(\theta, \zeta) \to (-\theta, -\zeta)$. The quantity $\mathcal{R}$ can be written as in (D 6) and the derivative with respect to a stellarator-asymmetric mode is

$$\frac{\partial\mathcal{R}}{\partial B^s_{mn}} = V'(\psi)^{-1} \int_0^{2\pi} \mathrm{d}\zeta \int_0^{2\pi} \mathrm{d}\theta \left(\sum_s \frac{\delta D_s}{\delta B} - \mathcal{R}\frac{\delta\sqrt{g}}{\delta B} \right) \sin(m\theta - n\zeta). \tag{D 11}$$

The functional derivative with respect to B does not change the parity of D_s or $\sqrt{g}$, thus we see that the quantity in parenthesis in the above equation is even with respect to the transformation $(\theta, \zeta) \to (-\theta, -\zeta)$. Therefore, $\partial\mathcal{R}/\partial B^s_{mn} = 0$ for all m and n. A similar argument cannot be made if $E_r \neq 0$, as the inhomogeneous drive term in (A 1) no longer has definite parity. However, according to the arguments in (Hirshman, Shaing & Van Rij 1986*a*) the transport coefficients do obey this symmetry property.

Appendix E. Derivatives at ambipolarity

In this appendix we derive an expression for derivatives of moments of the distribution function at fixed ambipolarity rather than fixed E_r by determining the relationship between geometry parameters, Ω, and E_r. To begin, it is assumed that the continuous adjoint approach outlined in § 3.1 is used. The approach taken here is analogous to that used in appendix A of Paul *et al.* (2018), in which an additional adjoint equation is used to compute derivatives at a fixed constraint function for optimization of stellarator coil shapes.

https://doi.org/10.1017/S0022377819000527 Published online by Cambridge University Press

Consider the set of unknowns computed with SFINCS, F, which depends on parameters Ω and E_r. The total differential of F satisfies

$$\mathbb{L}\mathrm{d}F(\Omega, E_r) = \left(\frac{\partial \mathbb{S}}{\partial E_r} - \frac{\partial \mathbb{L}}{\partial E_r}F\right)\mathrm{d}E_r + \sum_{i=1}^{N_\Omega}\left(\frac{\partial \mathbb{S}}{\partial \Omega_i} - \frac{\partial \mathbb{L}}{\partial \Omega_i}F\right)\mathrm{d}\Omega_i, \tag{E 1}$$

which follows from (2.11). Consider $J_r(F, \Omega)$, which depends on E_r through F. The total differential of J_r can be computed,

$$\mathrm{d}J_r(F(\Omega, E_r), \Omega) = \sum_{i=1}^{N_\Omega}\left(\frac{\partial J_r}{\partial \Omega_i}\right)_F + \langle \widetilde{J}_r, \mathrm{d}F(\Omega, E_r)\rangle, \tag{E 2}$$

which can be written using (E 1) and the solution to (5.11),

$$\begin{aligned}\mathrm{d}J_r(F(\Omega, E_r), \Omega) \;=\; &\left\langle q^{J_r}, \left(\frac{\partial \mathbb{S}}{\partial E_r} - \frac{\partial \mathbb{L}}{\partial E_r}F\right)\right\rangle \mathrm{d}E_r \\ &+ \sum_{i=1}^{N_\Omega}\left(\left(\frac{\partial J_r}{\partial \Omega_i}\right)_F + \left\langle q^{J_r}, \left(\frac{\partial \mathbb{S}}{\partial \Omega_i} - \frac{\partial \mathbb{L}}{\partial \Omega_i}F\right)\right\rangle\right)\mathrm{d}\Omega_i.\end{aligned} \tag{E 3}$$

By enforcing $\mathrm{d}J_r(F(\Omega, E_r), \Omega) = 0$, we obtain the relationship between E_r and Ω at ambipolarity,

$$\left(\frac{\partial E_r}{\partial \Omega_i}\right)_{J_r} = -\left\langle q^{J_r}, \left(\frac{\partial \mathbb{S}}{\partial E_r} - \frac{\partial \mathbb{L}}{\partial E_r}F\right)\right\rangle^{-1}\left(\left(\frac{\partial J_r}{\partial \Omega_i}\right)_F + \left\langle q^{J_r}, \left(\frac{\partial \mathbb{S}}{\partial \Omega_i} - \frac{\partial \mathbb{L}}{\partial \Omega_i}F\right)\right\rangle\right). \tag{E 4}$$

Consider a moment of the distribution function, $\mathcal{R}(F, \Omega)$. The derivative with respect to Ω_i at fixed ambipolarity can thus be computed,

$$\left(\frac{\partial \mathcal{R}}{\partial \Omega_i}\right)_{J_r} = \left(\frac{\partial \mathcal{R}}{\partial \Omega_i}\right)_{F,E_r} + \left\langle \widetilde{\mathcal{R}}, \left(\frac{\partial F}{\partial \Omega_i}\right)_{J_r}\right\rangle. \tag{E 5}$$

The first term corresponds to the explicit dependence on Ω_i, while the second contains dependence through F. Here $(\partial F/\partial \Omega_i)_{J_r}$ satisfies,

$$\begin{aligned}\mathbb{L}\left(\frac{\partial F}{\partial \Omega_i}\right)_{J_r} \;=\; &-\left(\frac{\partial \mathbb{S}}{\partial E_r} - \frac{\partial \mathbb{L}}{\partial E_r}F\right)\left\langle q^{J_r}, \left(\frac{\partial \mathbb{S}}{\partial E_r} - \frac{\partial \mathbb{L}}{\partial E_r}F\right)\right\rangle^{-1} \\ &\times\left(\left(\frac{\partial J_r}{\partial \Omega_i}\right)_F + \left\langle q^{J_r}, \left(\frac{\partial \mathbb{S}}{\partial \Omega_i} - \frac{\partial \mathbb{L}}{\partial \Omega_i}F\right)\right\rangle\right) + \left(\frac{\partial \mathbb{S}}{\partial \Omega_i} - \frac{\partial \mathbb{L}}{\partial \Omega_i}F\right),\end{aligned} \tag{E 6}$$

from (E 1) using (E 4). Using (E 6) and (3.7), we find

$$\begin{aligned}\left(\frac{\partial \mathcal{R}}{\partial \Omega_i}\right)_{J_r} = &\left(\frac{\partial \mathcal{R}}{\partial \Omega_i}\right)_{F,E_r} + \left\langle q^{\mathcal{R}}, \left(\frac{\partial \mathbb{S}}{\partial \Omega_i} - \frac{\partial \mathbb{L}}{\partial \Omega_i}F\right)\right\rangle \\ &- \left\langle q^{\mathcal{R}}, \left(\frac{\partial \mathbb{S}}{\partial E_r} - \frac{\partial \mathbb{L}}{\partial E_r}F\right)\right\rangle \frac{\left(\left(\frac{\partial J_r}{\partial \Omega_i}\right)_F + \left\langle q^{J_r}, \left(\frac{\partial \mathbb{S}}{\partial \Omega_i} - \frac{\partial \mathbb{L}}{\partial \Omega_i}F\right)\right\rangle\right)}{\left\langle q^{J_r}, \left(\frac{\partial \mathbb{S}}{\partial E_r} - \frac{\partial \mathbb{L}}{\partial E_r}F\right)\right\rangle}.\end{aligned} \tag{E 7}$$

https://doi.org/10.1017/S0022377819000527 Published online by Cambridge University Press

An analogous expression can be obtained using the discrete approach,

$$\left(\frac{\partial \mathcal{R}}{\partial \Omega_i}\right)_{J_r} = \left(\frac{\partial \mathcal{R}}{\partial \Omega_i}\right)_{F,E_r} + \left\langle \overrightarrow{\boldsymbol{q}}^{\mathcal{R}}, \left(\frac{\partial \overrightarrow{\boldsymbol{S}}}{\partial \Omega_i} - \frac{\partial \overleftrightarrow{\boldsymbol{L}}}{\partial \Omega_i}\overrightarrow{\boldsymbol{F}}\right)\right\rangle - \left\langle \overrightarrow{\boldsymbol{q}}^{\mathcal{R}}, \left(\frac{\partial \overrightarrow{\boldsymbol{S}}}{\partial E_r} - \frac{\partial \overleftrightarrow{\boldsymbol{L}}}{\partial E_r}\overrightarrow{\boldsymbol{F}}\right)\right\rangle \frac{\left(\left(\frac{\partial J_r}{\partial \Omega_i}\right)_F + \left\langle \overrightarrow{\boldsymbol{q}}^{J_r}, \left(\frac{\partial \overrightarrow{\boldsymbol{S}}}{\partial \Omega_i} - \frac{\partial \overleftrightarrow{\boldsymbol{L}}}{\partial \Omega_i}\overrightarrow{\boldsymbol{F}}\right)\right\rangle\right)}{\left\langle \overrightarrow{\boldsymbol{q}}^{J_r}, \left(\frac{\partial \overrightarrow{\boldsymbol{S}}}{\partial E_r} - \frac{\partial \overleftrightarrow{\boldsymbol{L}}}{\partial E_r}\overrightarrow{\boldsymbol{F}}\right)\right\rangle}, \tag{E 8}$$

where (5.12) has been used.

REFERENCES

Abel, I., Plunk, G., Wang, E., Barnes, M., Cowley, S., Dorland, W. & Schekochihin, A. 2013 Multiscale gyrokinetics for rotating tokamak plasmas: fluctuations, transport and energy flows. *Rep. Prog. Phys.* **76** (11), 116201.

Allaire, G., De Gournay, F., Jouve, F. & Toader, A.-M. 2005 Structural optimization using topological and shape sensitivity via a level set method. *Control and Cybernetics* **34** (1), 59.

Antonsen, T., Paul, E. J. & Landreman, M. 2019 Adjoint approach to calculating shape gradients for three-dimensional magnetic confinement equilibria. *J. Plasma Phys.* **85** (2), 905850207.

Barnes, M., Abel, I., Dorland, W., Görler, T., Hammett, G. & Jenko, F. 2010 Direct multiscale coupling of a transport code to gyrokinetic turbulence codes. *Phys. Plasmas* **17** (5), 056109.

Beidler, C., Allmaier, K., Isaev, M. Y., Kasilov, S., Kernbichler, W., Leitold, G., Maaßberg, H., Mikkelsen, D., Murakami, S., Schmidt, M. *et al.* 2011 Benchmarking of the mono-energetic transport coefficientsresults from the International Collaboration on Neoclassical Transport in Stellarators (ICNTS). *Nucl. Fusion* **51** (7), 076001.

Beidler, C., Grieger, G., Herrnegger, F., Harmeyer, E., Lotz, W., Maassberg, H., Merkel, P., Nührenberg, J., Rau, F., Sapper, J. *et al.* 1990 Physics and engineering design for Wendelstein VII-X. *Fusion Technol.* **17** (1), 148–168.

Beidler, C. D. & D'haeseleer, W. D. 1995 A general solution of the ripple-averaged kinetic equation (GSRAKE). *Plasma Phys. Control. Fusion* **37** (4), 463.

Belli, E. A. & Candy, J. 2015 Neoclassical transport in toroidal plasmas with nonaxisymmetric flux surfaces. *Plasma Phys. Control. Fusion* **57** (5), 054012.

Brent, R. P. 2013 *Algorithms for Minimization without Derivatives*. Courier Corporation.

Calvo, I., Velasco, J. L., Parra, F. I., Alonso, J. A. & García-Regaña, J. M. 2018 Electrostatic potential variations on stellarator magnetic surfaces in low collisionality regimes. *J. Plasma Phys.* **84** (4), 905840407.

Dekeyser, W., Reiter, D. & Baelmans, M. 2014*a* Automated divertor target design by adjoint shape sensitivity analysis and a one-shot method. *J. Comput. Phys.* **278**, 117–132.

Dekeyser, W., Reiter, D. & Baelmans, M. 2014*b* A one shot method for divertor target shape optimization. *Proc. Appl. Maths Mech.* **14** (1), 1017–1022.

Dekeyser, W., Reiter, D. & Baelmans, M. 2014*c* Optimal shape design for divertors. *Intl J. Comput. Sci. Eng. 2* **9** (5–6), 397–407.

Delfour, M. C. & Zolâsio, J.-P. 2011 *Shapes and Geometries: Metrics, Analysis, Differential Calculus, and Optimization*, Advances in Design and Control, vol. 22, chap. 2. SIAM.

Delfour, M. C. & Zolésio, J.-P. 2011 *Shapes and Geometries: Metrics, Analysis, Differential Calculus, and Optimization*, Advances in Design and Control, vol. 22, chap. 9. SIAM.

Fichtner, A., Bunge, H.-P. & Igel, H. 2006 The adjoint method in seismology: I. Theory. *Phys. Earth Planet. Inter.* **157** (1–2), 86–104.

Garren, D. & Boozer, A. H. 1991 Existence of quasihelically symmetric stellarators. *Phys. Fluids* B **3** (10), 2822–2834.

https://doi.org/10.1017/S0022377819000527 Published online by Cambridge University Press

GIBSON, A. & TAYLOR, J. B. 1967 Single particle motion in toroidal stellarator fields. *Phys. Fluids* **10** (12), 2653–2659.

GLOWINSKI, R. & PIRONNEAU, O. 1975 On the numerical computation of the minimum-drag profile in laminar flow. *J. Fluid Mech.* **72** (2), 385.

GRIEGER, G., LOTZ, W., MERKEL, P., NÜHRENBERG, J., SAPPER, J., STRUMBERGER, E., WOBIG, H., BURHENN, R., ERCKMANN, V., GASPARINO, U. *et al.* 1992 Physics optimization of stellarators. *Phys. Fluids* B **4** (7), 2081–2091.

HASTINGS, D., HOULBERG, W. & SHAING, K.-C. 1985 The ambipolar electric field in stellarators. *Nucl. Fusion* **25** (4), 445.

HELANDER, P. 2014 Theory of plasma confinement in non-axisymmetric magnetic fields. *Rep. Prog. Phys.* **77** (8), 087001.

HELANDER, P., PARRA, F. & NEWTON, S. 2017 Stellarator bootstrap current and plasma flow velocity at low collisionality. *J. Plasma Phys.* **83** (2), 905830206.

HENNEBERG, S., DREVLAK, M., NÜHRENBERG, C., BEIDLER, C., TURKIN, Y., LOIZU, J. & HELANDER, P. 2019 Properties of a new quasi-axisymmetric configuration. *Nucl. Fusion* **59** (2), 026014.

HIGHCOCK, E., MANDELL, N., BARNES, M. & DORLAND, W. 2018 Optimisation of confinement in a fusion reactor using a nonlinear turbulence model. *J. Plasma Phys.* **84** (2), 905840208.

HIRSHMAN, S., SHAING, K. & VAN RIJ, W. 1986*a* Consequences of time-reversal symmetry for the electric field scaling of transport in stellarators. *Phys. Rev. Lett.* **56** (16), 1697.

HIRSHMAN, S. P., SHAING, K. C., VAN RIJ, W. I., BEASLEY, C. O. & CRUME, E. C. 1986*b* Plasma transport coefficients for nonsymmetric toroidal confinement systems. *Phys. Fluids* **29** (9), 2951–2959.

HIRSHMAN, S., SPONG, D., WHITSON, J., NELSON, B., BATCHELOR, D., LYON, J., SANCHEZ, R., BROOKS, A., Y.-FU, G., GOLDSTON, R. *et al.* 1999 Physics of compact stellarators. *Phys. Plasmas* **6** (5), 1858–1864.

HIRSHMAN, S. P. & WHITSON, J. 1983 Steepest-descent moment method for three-dimensional magnetohydrodynamic equilibria. *Phys. Fluids* **26** (12), 3553–3568.

KERNBICHLER, W., KASILOV, S., KAPPER, G., MARTITSCH, A. F., NEMOV, V., ALBERT, C. & HEYN, M. 2016 Solution of drift kinetic equation in stellarators and tokamaks with broken symmetry using the code NEO-2. *Plasma Phys. Control. Fusion* **58** (10), 104001.

KROMMES, J. A. & HU, G. 1994 The role of dissipation in the theory and simulations of homogeneous plasma turbulence, and resolution of the entropy paradox. *Phys. Plasmas* **1** (10), 3211–3238.

KU, L., GARABEDIAN, P., LYON, J., TURNBULL, A., GROSSMAN, A., MAU, T., ZARNSTORFF, M. & TEAM, A. 2008 Physics design for ARIES-CS. *Fusion Sci. Technol.* **54** (3), 673–693.

LANDREMAN, M. & PAUL, E. J. 2018 Computing local sensitivity and tolerances for stellarator physics properties using shape gradients. *Nucl. Fusion* **58** (7), 076023.

LANDREMAN, M., PLUNK, G. G. & DORLAND, W. 2015 Generalized universal instability: transient linear amplification and subcritical turbulence. *J. Plasma Phys.* **81** (5), 905810501.

LANDREMAN, M. & SENGUPTA, W. 2018 Direct construction of optimized stellarator shapes. Part 1. Theory in cylindrical coordinates. *J. Plasma Phys.* **84** (6), 905840616.

LANDREMAN, M., SMITH, H. M., MOLLÉN, A. & HELANDER, P. 2014 Comparison of particle trajectories and collision operators for collisional transport in nonaxisymmetric plasmas. *Phys. Plasmas* **21** (4), 042503.

LOTZ, W., NÜHRENBERG, J. & SCHWAB, C. 1990 Optimization, MHD mode and alpha particle confinement behaviour of Helias equilibria. In *Plasma Physics and Controlled Nuclear Fusion Research*, vol. 2. International Atomic Energy Agency.

MAASSBERG, H., LOTZ, W. & NÜHRENBERG, J. 1993 Neoclassical bootstrap current and transport in optimized stellarator configurations. *Phys. Fluids* B **5** (10), 3728–3736.

NELSON, B., BERRY, L., BROOKS, A., COLE, M., CHRZANOWSKI, J., FAN, H.-M., FOGARTY, P., GORANSON, P., HEITZENROEDER, P., HIRSHMAN, S. *et al.* 2003 Design of the National Compact Stellarator Experiment (NCSX). *Fusion Engng Des.* **66**, 169–174.

https://doi.org/10.1017/S0022377819000527 Published online by Cambridge University Press

NEMOV, V., KASILOV, S., KERNBICHLER, W. & HEYN, M. 1999 Evaluation of $1/\nu$ neoclassical transport in stellarators. *Phys. Plasmas* **6** (12), 4622–4632.

NOCEDAL, J. & WRIGHT, S. J. 1999 *Numerical Optimization*, chap. 6. Springer.

NÜHRENBERG, J. & ZILLE, R. 1988 Quasi-helically symmetric toroidal stellarators. *Phys. Lett.* A **129**, 113–117.

PAUL, E. J., LANDREMAN, M., BADER, A. & DORLAND, W. 2018 An adjoint method for gradient-based optimization of stellarator coil shapes. *Nucl. Fusion* **58** (7), 076015.

PAUL, E. J., LANDREMAN, M., POLI, F. M., SPONG, D. A., SMITH, H. M. & DORLAND, W. 2017 Rotation and neoclassical ripple transport in ITER. *Nucl. Fusion* **57** (11), 116044.

PIERCE, N. A. & GILES, M. B. 2004 Adjoint and defect error bounding and correction for functional estimates. *J. Comput. Phys.* **200**, 769–794.

PIRONNEAU, O. 1974 On optimum design in fluid mechanics. *J. Fluid Mech.* **64** (1), 97–110.

PLESSIX, R.-E. 2006 A review of the adjoint-state method for computing the gradient of a functional with geophysical applications. *Geophys. J. Intl* **167** (2), 495–503.

PRESS, W. H., TEUKOLSKY, S. A., VETTERLING, W. T. & FLANNERY, B. P. 2007 *Numerical Recipes 3rd Edition: The Art of Scientific Computing*, chap. 9. Cambridge University Press.

REIMAN, A., FU, G., HIRSHMAN, S., KU, L., MONTICELLO, D., MYNICK, H., REDI, M., SPONG, D., ZARNSTORFF, M., BLACKWELL, B. *et al.* 1999 Physics design of a high-quasi-axisymmetric stellarator. *Plasma Phys. Control. Fusion* **41** (12B), B273.

VAN RIJ, W. I. & HIRSHMAN, S. P. 1989 Variational bounds for transport coefficients in three-dimensional toroidal plasmas. *Phys. Fluids* B **1** (3), 563–569.

ROSENBLUTH, M., HAZELTINE, R. & HINTON, F. L. 1972 Plasma transport in toroidal confinement systems. *Phys. Fluids* **15** (1), 116–140.

RUDIN, W. 2006 *Real and Complex Analysis*, chap. 4. Tata McGraw-Hill Education.

SANCHEZ, R., HIRSHMAN, S., WARE, A., BERRY, L. & SPONG, D. 2000 Ballooning stability optimization of low-aspect-ratio stellarators. *Plasma Phys. Control. Fusion* **42** (6), 641.

SAUER, T. 2012 *Numerical Analysis*, chap. 5. Pearson.

SHAING, K.-C., CRUME, E. JR, TOLLIVER, J., HIRSHMAN, S. & VAN RIJ, W. 1989 Bootstrap current and parallel viscosity in the low collisionality regime in toroidal plasmas. *Phys. Fluids* B **1** (1), 148–152.

SPONG, D., HIRSHMAN, S., WHITSON, J., BATCHELOR, D., CARRERAS, B., LYNCH, V. & ROME, J. 1998 J^* optimization of small aspect ratio stellarator/tokamak hybrid devices. *Phys. Plasmas* **5** (5), 1752–1758.

STRICKLER, D. J., HIRSHMAN, S. P., SPONG, D. A., COLE, M. J., LYON, J. F., NELSON, B. E., WILLIAMSON, D. E. & WARE, A. S. 2004 Development of a robust quasi-poloidal compact stellarator. *Fusion Sci. Technol.* **45** (1), 15–26.

SUGAMA, H., WATANABE, T.-H. & NUNAMI, M. 2009 Linearized model collision operators for multiple ion species plasmas and gyrokinetic entropy balance equations. *Phys. Plasmas* **16** (11), 112503.

VENDITTI, D. & DARMOFAL, D. 1999 A multilevel error estimation and grid adaptive strategy for improving the accuracy of integral outputs. In *14th Computational Fluid Dynamics Conference*, p. 3292.

ZARNSTORFF, M., BERRY, L., BROOKS, A., FREDRICKSON, E., FU, G., HIRSHMAN, S., HUDSON, S., KU, L., LAZARUS, E., MIKKELSEN, D. *et al.* 2001 Physics of the compact advanced stellarator NCSX. *Plasma Phys. Control. Fusion* **43** (12A), A237.

https://doi.org/10.1017/S0022377819000527 Published online by Cambridge University Press